

Observation of $e^+e^- \rightarrow \pi^+\pi^-\psi(3770)$ and $D_1(2420)^0\bar{D}^0 + c.c.$

M. Ablikim¹, M. N. Achasov^{10,d}, P. Adlarson⁵⁹, S. Ahmed¹⁵, M. Albrecht⁴, M. Alekseev^{58A,58C}, A. Amoroso^{58A,58C}, F. F. An¹, Q. An^{55,43}, Y. Bai⁴², O. Bakina²⁷, R. Baldini Ferroli^{23A}, I. Balossino Balossino^{24A}, Y. Ban³⁵, K. Begzsuren²⁵, J. V. Bennett⁵, N. Berger²⁶, M. Bertani^{23A}, D. Bettoni^{24A}, F. Bianchi^{58A,58C}, J. Biernat⁵⁹, J. Bloms⁵², I. Boyko²⁷, R. A. Briere⁵, H. Cai⁶⁰, X. Cai^{1,43}, A. Calcaterra^{23A}, G. F. Cao^{1,47}, N. Cao^{1,47}, S. A. Cetin^{46B}, J. Chai^{58C}, J. F. Chang^{1,43}, W. L. Chang^{1,47}, G. Chelkov^{27,b,c}, D. Y. Chen⁶, G. Chen¹, H. S. Chen^{1,47}, J. C. Chen¹, M. L. Chen^{1,43}, S. J. Chen³³, Y. B. Chen^{1,43}, W. Cheng^{58C}, G. Cibinetto^{24A}, F. Cossio^{58C}, X. F. Cui³⁴, H. L. Dai^{1,43}, J. P. Dai^{38,h}, X. C. Dai^{1,47}, A. Dbeysi¹⁵, D. Dedovich²⁷, Z. Y. Deng¹, A. Denig²⁶, I. Denysenko²⁷, M. Destefanis^{58A,58C}, F. De Mori^{58A,58C}, Y. Ding³¹, C. Dong³⁴, J. Dong^{1,43}, L. Y. Dong^{1,47}, M. Y. Dong^{1,43,47}, Z. L. Dou³³, S. X. Du⁶³, J. Z. Fan⁴⁵, J. Fang^{1,43}, S. S. Fang^{1,47}, Y. Fang¹, R. Farinelli^{24A,24B}, L. Fava^{58B,58C}, F. Feldbauer⁴, G. Felici^{23A}, C. Q. Feng^{55,43}, M. Fritsch⁴, C. D. Fu¹, Y. Fu¹, Q. Gao¹, X. L. Gao^{55,43}, Y. Gao⁴⁵, Y. Gao⁵⁶, Y. G. Gao⁶, Z. Gao^{55,43}, B. Garillon²⁶, I. Garzia^{24A}, E. M. Gersabeck⁵⁰, A. Gilman⁵¹, K. Goetzen¹¹, L. Gong³⁴, W. X. Gong^{1,43}, W. Gradl²⁶, M. Greco^{58A,58C}, L. M. Gu³³, M. H. Gu^{1,43}, S. Gu², Y. T. Gu¹³, A. Q. Guo²², L. B. Guo³², R. P. Guo³⁶, Y. P. Guo²⁶, A. Guskov²⁷, S. Han⁶⁰, X. Q. Hao¹⁶, F. A. Harris⁴⁸, K. L. He^{1,47}, F. H. Heinsius⁴, T. Held⁴, Y. K. Heng^{1,43,47}, M. Himmelreich^{11,g}, Y. R. Hou⁴⁷, Z. L. Hou¹, H. M. Hu^{1,47}, J. F. Hu^{38,h}, T. Hu^{1,43,47}, Y. Hu¹, G. S. Huang^{55,43}, J. S. Huang¹⁶, X. T. Huang³⁷, X. Z. Huang³³, N. Huesken⁵², T. Hussain⁵⁷, W. Ikegami Andersson⁵⁹, W. Imoehl²², M. Irshad^{55,43}, Q. Ji¹, Q. P. Ji¹⁶, X. B. Ji^{1,47}, X. L. Ji^{1,43}, H. L. Jiang³⁷, X. S. Jiang^{1,43,47}, X. Y. Jiang³⁴, J. B. Jiao³⁷, Z. Jiao¹⁸, D. P. Jin^{1,43,47}, S. Jin³³, Y. Jin⁴⁹, T. Johansson⁵⁹, N. Kalantar-Nayestanaki²⁹, X. S. Kang³¹, R. Kappert²⁹, M. Kavatsyuk²⁹, B. C. Ke¹, I. K. Keshk⁴, A. Khoukaz⁵², P. Kiese²⁶, R. Kiuchi¹, R. Kliemt¹¹, L. Koch²⁸, O. B. Kolcu^{46B,f}, B. Kopf⁴, M. Kuemmel⁴, M. Kuessner⁴, A. Kupsc⁵⁹, M. Kurth¹, M. G. Kurth^{1,47}, W. Kühn²⁸, J. S. Lange²⁸, P. Larin¹⁵, L. Lavezzi^{58C}, H. Leithoff²⁶, T. Lenz²⁶, C. Li⁵⁹, Cheng Li^{55,43}, D. M. Li⁶³, F. Li^{1,43}, F. Y. Li³⁵, G. Li¹, H. B. Li^{1,47}, H. J. Li^{9,j}, J. C. Li¹, J. W. Li⁴¹, Ke Li¹, L. K. Li¹, Lei Li³, P. L. Li^{55,43}, P. R. Li³⁰, Q. Y. Li³⁷, W. D. Li^{1,47}, W. G. Li¹, X. H. Li^{55,43}, X. L. Li³⁷, X. N. Li^{1,43}, Z. B. Li⁴⁴, Z. Y. Li⁴⁴, H. Liang^{1,47}, H. Liang^{55,43}, Y. F. Liang⁴⁰, Y. T. Liang²⁸, G. R. Liao¹², L. Z. Liao^{1,47}, J. Libby²¹, C. X. Lin⁴⁴, D. X. Lin¹⁵, Y. J. Lin¹³, B. Liu^{38,h}, B. J. Liu¹, C. X. Liu¹, D. Liu^{55,43}, D. Y. Liu^{38,h}, F. H. Liu³⁹, Fang Liu¹, Feng Liu⁶, H. B. Liu¹³, H. M. Liu^{1,47}, Huanhuan Liu¹, Huihui Liu¹⁷, J. B. Liu^{55,43}, J. Y. Liu^{1,47}, K. Y. Liu³¹, Ke Liu⁶, L. Y. Liu¹³, Q. Liu⁴⁷, S. B. Liu^{55,43}, T. Liu^{1,47}, X. Liu³⁰, X. Y. Liu^{1,47}, Y. B. Liu³⁴, Z. A. Liu^{1,43,47}, Zhiqing Liu³⁷, Y. F. Long³⁵, X. C. Lou^{1,43,47}, H. J. Lu¹⁸, J. D. Lu^{1,47}, J. G. Lu^{1,43}, Y. Lu¹, Y. P. Lu^{1,43}, C. L. Luo³², M. X. Luo⁶², P. W. Luo⁴⁴, T. Luo^{9,j}, X. L. Luo^{1,43}, S. Lusso^{58C}, X. R. Lyu⁴⁷, F. C. Ma³¹, H. L. Ma¹, L. L. Ma³⁷, M. M. Ma^{1,47}, Q. M. Ma¹, X. N. Ma³⁴, X. X. Ma^{1,47}, X. Y. Ma^{1,43}, Y. M. Ma³⁷, F. E. Maas¹⁵, M. Maggiora^{58A,58C}, S. Maldaner²⁶, S. Malde⁵³, Q. A. Malik⁵⁷, A. Mangoni^{23B}, Y. J. Mao³⁵, Z. P. Mao¹, S. Marcello^{58A,58C}, Z. X. Meng⁴⁹, J. G. Messchendorp²⁹, G. Mezzadri^{24A}, J. Min^{1,43}, T. J. Min³³, R. E. Mitchell²², X. H. Mo^{1,43,47}, Y. J. Mo⁶, C. Morales Morales¹⁵, N. Yu. Muchnoi^{10,d}, H. Muramatsu⁵¹, A. Mustafa⁴, S. Nakhoul^{11,g}, Y. Nefedov²⁷, F. Nerling^{11,g}, I. B. Nikolaev^{10,d}, Z. Ning^{1,43}, S. Nisar^{8,k}, S. L. Niu^{1,43}, S. L. Olsen⁴⁷, Q. Ouyang^{1,43,47}, S. Pacetti^{23B}, Y. Pan^{55,43}, M. Papenbrock⁵⁹, P. Patteri^{23A}, M. Pelizaeus⁴, H. P. Peng^{55,43}, K. Peters^{11,g}, J. Pettersson⁵⁹, J. L. Ping³², R. G. Ping^{1,47}, A. Pitka⁴, R. Poling⁵¹, V. Prasad^{55,43}, M. Qi³³, T. Y. Qi², S. Qian^{1,43}, C. F. Qiao⁴⁷, N. Qin⁶⁰, X. P. Qin¹³, X. S. Qin⁴, Z. H. Qin^{1,43}, J. F. Qiu¹, S. Q. Qu³⁴, K. H. Rashid^{57,i}, C. F. Redmer²⁶, M. Richter⁴, A. Rivetti^{58C}, V. Rodin²⁹, M. Rolo^{58C}, G. Rong^{1,47}, Ch. Rosner¹⁵, M. Rump⁵², A. Sarantsev^{27,e}, M. Savri^{24B}, K. Schoenning⁵⁹, W. Shan¹⁹, X. Y. Shan^{55,43}, M. Shao^{55,43}, C. P. Shen², P. X. Shen³⁴, X. Y. Shen^{1,47}, H. Y. Sheng¹, X. Shi^{1,43}, X. D. Shi^{55,43}, J. J. Song³⁷, Q. Q. Song^{55,43}, W. M. Song¹, X. Y. Song¹, S. Sosio^{58A,58C}, C. Sowa⁴, S. Spataro^{58A,58C}, F. F. Sul³⁷, G. X. Sun¹, J. F. Sun¹⁶, L. Sun⁶⁰, S. S. Sun^{1,47}, X. H. Sun¹, Y. J. Sun^{55,43}, Y. K. Sun^{55,43}, Y. Z. Sun¹, Z. J. Sun^{1,43}, Z. T. Sun¹, Y. T. Tan^{55,43}, C. J. Tang⁴⁰, G. Y. Tang¹, X. Tang¹, V. Thoren⁵⁹, B. Tsednee²⁵, I. Uman^{46D}, B. Wang¹, B. L. Wang⁴⁷, C. W. Wang³³, D. Y. Wang³⁵, H. H. Wang³⁷, K. Wang^{1,43}, L. L. Wang¹, L. S. Wang¹, M. Wang³⁷, M. Z. Wang³⁵, Meng Wang^{1,47}, P. L. Wang¹, R. M. Wang⁶¹, W. P. Wang^{55,43}, X. Wang³⁵, X. F. Wang¹, X. L. Wang^{9,j}, Y. Wang⁴⁴, Y. Wang^{55,43}, Y. F. Wang^{1,43,47}, Z. Wang^{1,43}, Z. G. Wang^{1,43}, Z. Y. Wang¹, Zongyuan Wang^{1,47}, T. Weber⁴, D. H. Wei¹², P. Weidenkaff²⁶, H. W. Wen³², S. P. Wen¹, U. Wiedner⁴, G. Wilkinson⁵³, M. Wolke⁵⁹, L. H. Wu¹, L. J. Wu^{1,47}, Z. Wu^{1,43}, L. Xia^{55,43}, Y. Xia²⁰, S. Y. Xiao¹, Y. J. Xiao^{1,47}, Z. J. Xiao³², Y. G. Xie^{1,43}, Y. H. Xie⁶, T. Y. Xing^{1,47}, X. A. Xiong^{1,47}, Q. L. Xiu^{1,43}, G. F. Xu¹, J. J. Xu³³, L. Xu¹, Q. J. Xu¹⁴, W. Xu^{1,47}, X. P. Xu⁴¹, F. Yan⁵⁶, L. Yan^{58A,58C}, W. B. Yan^{55,43}, W. C. Yan², Y. H. Yan²⁰, H. J. Yang^{38,h}, H. X. Yang¹, L. Yang⁶⁰, R. X. Yang^{55,43}, S. L. Yang^{1,47}, Y. H. Yang³³, Y. X. Yang¹², Yifan Yang^{1,47}, Z. Q. Yang²⁰, M. Ye^{1,43}, M. H. Ye⁷, J. H. Yin¹, Z. Y. You⁴⁴, B. X. Yu^{1,43,47}, C. X. Yu³⁴, J. S. Yu²⁰, C. Z. Yuan^{1,47}, X. Q. Yuan³⁵, Y. Yuan¹, A. Yuncu^{46B,a}, A. A. Zafar⁵⁷, Y. Zeng²⁰, B. X. Zhang¹, B. Y. Zhang^{1,43}, C. C. Zhang¹, D. H. Zhang¹, H. H. Zhang⁴⁴, H. Y. Zhang^{1,43}, J. Zhang^{1,47}, J. L. Zhang⁶¹, J. Q. Zhang⁴, J. W. Zhang^{1,43,47}, J. Y. Zhang¹, J. Z. Zhang^{1,47}, K. Zhang^{1,47}, L. Zhang⁴⁵, S. F. Zhang³³, T. J. Zhang^{38,h}, X. Y. Zhang³⁷, Y. Zhang^{55,43}, Y. H. Zhang^{1,43}, Y. T. Zhang^{55,43}, Yang Zhang¹, Yao Zhang¹, Yi Zhang^{9,j}, Yu Zhang⁴⁷, Z. H. Zhang⁶, Z. P. Zhang⁵⁵, Z. Y. Zhang⁶⁰, G. Zhao¹, J. W. Zhao^{1,43}, J. Y. Zhao^{1,47}, J. Z. Zhao^{1,43}, Lei Zhao^{55,43},

Ling Zhao¹, M. G. Zhao³⁴, Q. Zhao¹, S. J. Zhao⁶³, T. C. Zhao¹, Y. B. Zhao^{1,43}, Z. G. Zhao^{55,43}, A. Zhemchugov^{27,b}, B. Zheng⁵⁶, J. P. Zheng^{1,43}, Y. Zheng³⁵, Y. H. Zheng⁴⁷, B. Zhong³², L. Zhou^{1,43}, L. P. Zhou^{1,47}, Q. Zhou^{1,47}, X. Zhou⁶⁰, X. K. Zhou⁴⁷, X. R. Zhou^{55,43}, Xiaoyu Zhou²⁰, Xu Zhou²⁰, A. N. Zhu^{1,47}, J. Zhu³⁴, J. Zhu⁴⁴, K. Zhu¹, K. J. Zhu^{1,43,47}, S. H. Zhu⁵⁴, W. J. Zhu³⁴, X. L. Zhu⁴⁵, Y. C. Zhu^{55,43}, Y. S. Zhu^{1,47}, Z. A. Zhu^{1,47}, J. Zhuang^{1,43}, B. S. Zou¹, J. H. Zou¹

(BESIII Collaboration)

- ¹ *Institute of High Energy Physics, Beijing 100049, People's Republic of China*
² *Beihang University, Beijing 100191, People's Republic of China*
³ *Beijing Institute of Petrochemical Technology, Beijing 102617, People's Republic of China*
⁴ *Bochum Ruhr-University, D-44780 Bochum, Germany*
⁵ *Carnegie Mellon University, Pittsburgh, Pennsylvania 15213, USA*
⁶ *Central China Normal University, Wuhan 430079, People's Republic of China*
⁷ *China Center of Advanced Science and Technology, Beijing 100190, People's Republic of China*
⁸ *COMSATS University Islamabad, Lahore Campus, Defence Road, Off Raiwind Road, 54000 Lahore, Pakistan*
⁹ *Fudan University, Shanghai 200443, People's Republic of China*
¹⁰ *G.I. Budker Institute of Nuclear Physics SB RAS (BINP), Novosibirsk 630090, Russia*
¹¹ *GSI Helmholtzcentre for Heavy Ion Research GmbH, D-64291 Darmstadt, Germany*
¹² *Guangxi Normal University, Guilin 541004, People's Republic of China*
¹³ *Guangxi University, Nanning 530004, People's Republic of China*
¹⁴ *Hangzhou Normal University, Hangzhou 310036, People's Republic of China*
¹⁵ *Helmholtz Institute Mainz, Johann-Joachim-Becher-Weg 45, D-55099 Mainz, Germany*
¹⁶ *Henan Normal University, Xinxiang 453007, People's Republic of China*
¹⁷ *Henan University of Science and Technology, Luoyang 471003, People's Republic of China*
¹⁸ *Huangshan College, Huangshan 245000, People's Republic of China*
¹⁹ *Hunan Normal University, Changsha 410081, People's Republic of China*
²⁰ *Hunan University, Changsha 410082, People's Republic of China*
²¹ *Indian Institute of Technology Madras, Chennai 600036, India*
²² *Indiana University, Bloomington, Indiana 47405, USA*
²³ (A) *INFN Laboratori Nazionali di Frascati, I-00044, Frascati, Italy*; (B) *INFN and University of Perugia, I-06100, Perugia, Italy*
²⁴ (A) *INFN Sezione di Ferrara, I-44122, Ferrara, Italy*; (B) *University of Ferrara, I-44122, Ferrara, Italy*
²⁵ *Institute of Physics and Technology, Peace Ave. 54B, Ulaanbaatar 13330, Mongolia*
²⁶ *Johannes Gutenberg University of Mainz, Johann-Joachim-Becher-Weg 45, D-55099 Mainz, Germany*
²⁷ *Joint Institute for Nuclear Research, 141980 Dubna, Moscow region, Russia*
²⁸ *Justus-Liebig-Universitaet Giessen, II. Physikalisches Institut, Heinrich-Buff-Ring 16, D-35392 Giessen, Germany*
²⁹ *KVI-CART, University of Groningen, NL-9747 AA Groningen, The Netherlands*
³⁰ *Lanzhou University, Lanzhou 730000, People's Republic of China*
³¹ *Liaoning University, Shenyang 110036, People's Republic of China*
³² *Nanjing Normal University, Nanjing 210023, People's Republic of China*
³³ *Nanjing University, Nanjing 210093, People's Republic of China*
³⁴ *Nankai University, Tianjin 300071, People's Republic of China*
³⁵ *Peking University, Beijing 100871, People's Republic of China*
³⁶ *Shandong Normal University, Jinan 250014, People's Republic of China*
³⁷ *Shandong University, Jinan 250100, People's Republic of China*
³⁸ *Shanghai Jiao Tong University, Shanghai 200240, People's Republic of China*
³⁹ *Shanxi University, Taiyuan 030006, People's Republic of China*
⁴⁰ *Sichuan University, Chengdu 610064, People's Republic of China*
⁴¹ *Soochow University, Suzhou 215006, People's Republic of China*
⁴² *Southeast University, Nanjing 211100, People's Republic of China*
⁴³ *State Key Laboratory of Particle Detection and Electronics, Beijing 100049, Hefei 230026, People's Republic of China*
⁴⁴ *Sun Yat-Sen University, Guangzhou 510275, People's Republic of China*
⁴⁵ *Tsinghua University, Beijing 100084, People's Republic of China*
⁴⁶ (A) *Ankara University, 06100 Tandogan, Ankara, Turkey*; (B) *Istanbul Bilgi University, 34060 Eyup, Istanbul, Turkey*; (C) *Uludag University, 16059 Bursa, Turkey*; (D) *Near East University, Nicosia, North Cyprus, Mersin 10, Turkey*

⁴⁷ *University of Chinese Academy of Sciences, Beijing 100049, People's Republic of China*

⁴⁸ *University of Hawaii, Honolulu, Hawaii 96822, USA*

⁴⁹ *University of Jinan, Jinan 250022, People's Republic of China*

⁵⁰ *University of Manchester, Oxford Road, Manchester, M13 9PL, United Kingdom*

⁵¹ *University of Minnesota, Minneapolis, Minnesota 55455, USA*

⁵² *University of Muenster, Wilhelm-Klemm-Str. 9, 48149 Muenster, Germany*

⁵³ *University of Oxford, Keble Rd, Oxford, UK OX13RH*

⁵⁴ *University of Science and Technology Liaoning, Anshan 114051, People's Republic of China*

⁵⁵ *University of Science and Technology of China, Hefei 230026, People's Republic of China*

⁵⁶ *University of South China, Hengyang 421001, People's Republic of China*

⁵⁷ *University of the Punjab, Lahore-54590, Pakistan*

⁵⁸ (A)*University of Turin, I-10125, Turin, Italy; (B)University of Eastern*

Piedmont, I-15121, Alessandria, Italy; (C)INFN, I-10125, Turin, Italy

⁵⁹ *Uppsala University, Box 516, SE-75120 Uppsala, Sweden*

⁶⁰ *Wuhan University, Wuhan 430072, People's Republic of China*

⁶¹ *Xinyang Normal University, Xinyang 464000, People's Republic of China*

⁶² *Zhejiang University, Hangzhou 310027, People's Republic of China*

⁶³ *Zhengzhou University, Zhengzhou 450001, People's Republic of China*

^a *Also at Bogazici University, 34342 Istanbul, Turkey*

^b *Also at the Moscow Institute of Physics and Technology, Moscow 141700, Russia*

^c *Also at the Functional Electronics Laboratory, Tomsk State University, Tomsk, 634050, Russia*

^d *Also at the Novosibirsk State University, Novosibirsk, 630090, Russia*

^e *Also at the NRC "Kurchatov Institute", PNPI, 188300, Gatchina, Russia*

^f *Also at Istanbul Arel University, 34295 Istanbul, Turkey*

^g *Also at Goethe University Frankfurt, 60323 Frankfurt am Main, Germany*

^h *Also at Key Laboratory for Particle Physics, Astrophysics and Cosmology, Ministry of Education; Shanghai Key Laboratory for Particle Physics and Cosmology; Institute of Nuclear and Particle Physics, Shanghai 200240, People's Republic of China*

ⁱ *Also at Government College Women University, Sialkot - 51310. Punjab, Pakistan.*

^j *Also at Key Laboratory of Nuclear Physics and Ion-beam Application (MOE) and Institute of Modern Physics, Fudan University, Shanghai 200443, People's Republic of China*

^k *Also at Harvard University, Department of Physics, Cambridge, MA, 02138, USA*

Several intermediate states of the reaction channels $e^+e^- \rightarrow \pi^+\pi^-D^0\bar{D}^0$ and $e^+e^- \rightarrow \pi^+\pi^-D^+D^-$ are studied using the data samples collected with the BESIII detector at center-of-mass energies above 4.08 GeV. For the first time in this final state, a $\psi(3770)$ signal is seen in the $D\bar{D}$ invariant mass spectrum, with a statistical significance of 5.2σ at $\sqrt{s} = 4.42$ GeV. There is also evidence for this resonance at $\sqrt{s} = 4.26$ and 4.36 GeV with statistical significance of 3.2σ and 3.3σ , respectively. In addition, the Born cross section of $e^+e^- \rightarrow \pi^+\pi^-\psi(3770)$ is measured. The proposed heavy-quark-spin-symmetry partner of the $X(3872)$, the state $X_2(4013)$, is also searched for in the $D\bar{D}$ invariant mass spectra. No obvious signal is found. The upper limit of the Born cross section of the process $e^+e^- \rightarrow \rho^0 X_2(4013)$ combined with the branching fraction is measured. Also, the processes $e^+e^- \rightarrow D_1(2420)\bar{D} + c.c.$ are investigated. The neutral mode with $D_1(2420)^0 \rightarrow D^0\pi^+\pi^-$ is reported with statistical significance of 7.4σ at $\sqrt{s} = 4.42$ GeV for the first time, and evidence with statistical significance of 3.2σ and 3.3σ at $\sqrt{s} = 4.36$ and 4.60 GeV is seen, respectively. No evident signal for the process $e^+e^- \rightarrow D_1(2420)^0\bar{D}^0 + c.c.$, $D_1(2420)^0 \rightarrow D^{*+}\pi^-$ is reported. Evidence for $e^+e^- \rightarrow D_1(2420)^+D^- + c.c.$, $D_1(2420)^+ \rightarrow D^+\pi^+\pi^-$ is reported with statistical significance of 3.1σ and 3.0σ at $\sqrt{s} = 4.36$ and 4.42 GeV, respectively.

PACS numbers: 14.40.Rt, 13.20.Gd, 13.66.Bc, 13.40.Hq, 14.40.Pq

I. INTRODUCTION

Heavy quarkonia have been studied for more than forty years for testing and developing quantum chromodynamics (QCD). On the one hand, some effective theories have been developed to describe quarkonium spectroscopy and transition

dynamics [1–3]; on the other hand, many XYZ particles were discovered [4–6], and some of them are beyond the scope of potential models. The rich information gained from the XYZ particles may have opened a door through which quark confinement can be understood [7, 8]. To understand these XYZ particles, it is of great importance to understand also the properties of the conventional quarkonia.

In recent years, several new vector charmonium-like states, the $Y(4260)$, $Y(4360)$, and $Y(4660)$, have been discovered via their decays into hidden-charm final states such as $\pi^+\pi^-J/\psi$ or $\pi^+\pi^-\psi(3686)$ [9–13]. The charged $Z_c(3900)$ s and similar structures have been observed in the $\pi^\pm J/\psi$ and $\pi^\pm\psi(3686)$ invariant mass spectra in the processes $e^+e^- \rightarrow \pi^+\pi^-J/\psi$ and $\pi^+\pi^-\psi(3686)$, respectively at BESIII, Belle, and with CLEO-c data [11, 12, 14–16]. A natural extension would be a search for the process $e^+e^- \rightarrow \pi^+\pi^-\psi(3770)$ and for the corresponding charged resonance that decays to $\pi^\pm\psi(3770)$.

The $\psi(3770)$ is generally assumed to be the 1^3D_1 charmonium state with some admixture of the 2^3S_1 state. One of the D -wave spin-triplet charmonium states, the $\psi(1^3D_2)$ or $X(3823)$, has recently been observed in $e^+e^- \rightarrow \pi^+\pi^-\psi(1^3D_2)$ at BESIII [17]. Therefore, the final states $\pi^+\pi^-\psi(3770)$ and $\pi^+\pi^-\psi(1^3D_3)$ should be produced at BESIII as well, although so far there is no calculation on how large the production rates could be. The $\psi(3770)$ decays dominantly to $D\bar{D}$, which is also expected to be an important decay mode of the $\psi(1^3D_3)$. The predicted mass of the $\psi(1^3D_3)$ is at 3849 MeV/ c^2 [18], however, there is no prediction for the width. Therefore, by studying the process $e^+e^- \rightarrow \pi\pi D\bar{D}$, one can also search for the $\psi(1^3D_3)$.

The $X(3872)$ state was first observed by Belle [19], and confirmed subsequently by several other experiments [20–22]. Even though it clearly contains a $c\bar{c}$ pair, the $X(3872)$ does not fit in the conventional charmonium spectrum. It could be interpreted as a $D\bar{D}^*$ molecule with $J^{PC} = 1^{++}$ [23, 24]. Throughout this paper, the charged conjugate mode is implied unless it is stated otherwise. Within this picture the existence of its heavy quark-spin-symmetry partner $X_2(4013)$ ($J^{PC} = 2^{++}$), an S -wave $D^*\bar{D}^*$ bound state, is predicted [25, 26]. Its mass and width are predicted as about 4013 MeV/ c^2 and ~ 2 -8 MeV, respectively. The $X_2(4013)$ is expected to decay dominantly to $D\bar{D}$ or $D\bar{D}^*$ in D -wave. So it may also be produced in $e^+e^- \rightarrow \pi^+\pi^-D\bar{D}$. The possible discovery of the 2^{++} charmonium-like state will provide a strong support for the interpretation that the $X(3872)$ is dominantly a $D\bar{D}^*$ hadronic molecule [27].

Amongst various models to interpret the $Y(4260)$ [9, 11], the authors of Ref. [28] argue that the $Y(4260)$ as a relative S -wave $D_1(2420)\bar{D}$ system is able to accommodate nearly all the present observations of the $Y(4260)$. Especially its absence in various open charm decay channels and the observation of the $Z_c(3900)$ in $Y(4260) \rightarrow \pi^+\pi^-J/\psi$ support this interpretation. In this model, the coupling strength of $D_1(2420)\bar{D}$ to $Y(4260)$ is a key piece of information. Because of $D_1(2420)$ decays to $D\pi\pi$ or $D^*\pi$, this can also be studied via the $\pi\pi D\bar{D}$ final state.

In this paper, we report the observation of $e^+e^- \rightarrow \pi^+\pi^-\psi(3770)$ and $D_1(2420)^0\bar{D}^0$ based on data samples collected with the BESIII detector from 2012 to 2014. The Born cross sections of $e^+e^- \rightarrow \pi^+\pi^-\psi(3770)$ at center-of-mass (c.m.) energies \sqrt{s} above 4.08 GeV, $e^+e^- \rightarrow \rho^0 X_2(4013)$ at $\sqrt{s} = 4.36, 4.42, \text{ and } 4.60$ GeV, and $e^+e^- \rightarrow D_1\bar{D}$ above 4.30 GeV are measured. The energies of the data samples used

in this analysis are 4.0854, 4.1886, 4.2077, 4.2171, 4.2263, 4.2417, 4.2580, 4.3079, 4.3583, 4.3874, 4.4156, 4.4671, 4.5271, 4.5745, 4.5995 GeV, respectively. To make the text easier to read, we use 4.09, 4.19, 4.21, 4.22, 4.23, 4.245, 4.26, 4.31, 4.36, 4.39, 4.42, 4.47, 4.53, 4.575 and 4.60 GeV in the following instead.

II. THE EXPERIMENT AND DATA SETS

The BESIII detector is a magnetic spectrometer [29] located at the Beijing Electron Positron Collider (BEPCII) [30]. The cylindrical core of the BESIII detector consists of a helium-based multilayer drift chamber (MDC), a plastic scintillator time-of-flight system (TOF), and a CsI(Tl) electromagnetic calorimeter (EMC), which are all enclosed in a superconducting solenoidal magnet providing a 1.0 T magnetic field. The solenoid is supported by an octagonal flux-return yoke with resistive plate counter muon identifier modules interleaved with steel. The acceptance of charged particles and photons is 93% over 4π solid angle. The charged-particle momentum resolution at 1 GeV/ c is 0.5%, and the specific energy loss (dE/dx) resolution is 6% for the electrons from Bhabha scattering. The EMC measures photon energies with a resolution of 2.5% (5%) at 1 GeV in the barrel (end cap) region. The time resolution of the TOF barrel part is 68 ps, while that of the end cap part is 110 ps.

For this analysis, the data sets above 4.08 GeV recorded with the BESIII detector are used. The c.m. energy and the corresponding integrated luminosity of each data sample are listed in Table I. The c.m. energy is measured using di-muon events with a precision of 0.8 MeV [31]. The integrated luminosity is determined by analyzing large-angle Bhabha scattering events. The uncertainty of the integrated luminosity is 1.0% [32].

Simulated data samples produced with the GEANT4-based [33] Monte Carlo (MC) package, which includes the geometric description of the BESIII detector and the detector response, are used to determine the detection efficiency and to estimate the background contributions. The simulation includes the beam energy spread and allows for the production of initial state radiation (ISR) photons in the e^+e^- annihilation process. Both effects are modeled within the generator package KKMC [34].

For the optimization of the selection criteria, the following MC samples with 200,000 events for each process are produced at each c.m. energy: $e^+e^- \rightarrow \pi^+\pi^-\psi(3770)$, with $\psi(3770) \rightarrow D\bar{D}$; $e^+e^- \rightarrow \rho^0 X_2(4013)$ with $\rho^0 \rightarrow \pi^+\pi^-$ and $X_2(4013) \rightarrow D\bar{D}$; $e^+e^- \rightarrow D_1(2420)^0\bar{D}^0$ with $D_1(2420)^0 \rightarrow D_0^*(2308)^+\pi^- \rightarrow D^0\pi^+\pi^-$ ($D_1 \rightarrow D\pi\pi$ decays through the quasi-two-body intermediate state $D_0^*(2308)$ [35]); $e^+e^- \rightarrow D_1(2420)^0\bar{D}^0$ with $D_1(2420)^0 \rightarrow D^{*+}\pi^-$; $e^+e^- \rightarrow D_1(2420)^+\bar{D}^-$ with $D_1(2420)^+ \rightarrow D_0^*(2308)^0\pi^+ \rightarrow D^+\pi^-\pi^+$. The width of $X_2(4013)$ and $D_0^*(2308)$ are set to 8 and 276 MeV, respectively.

In order to estimate the potential background contributions,

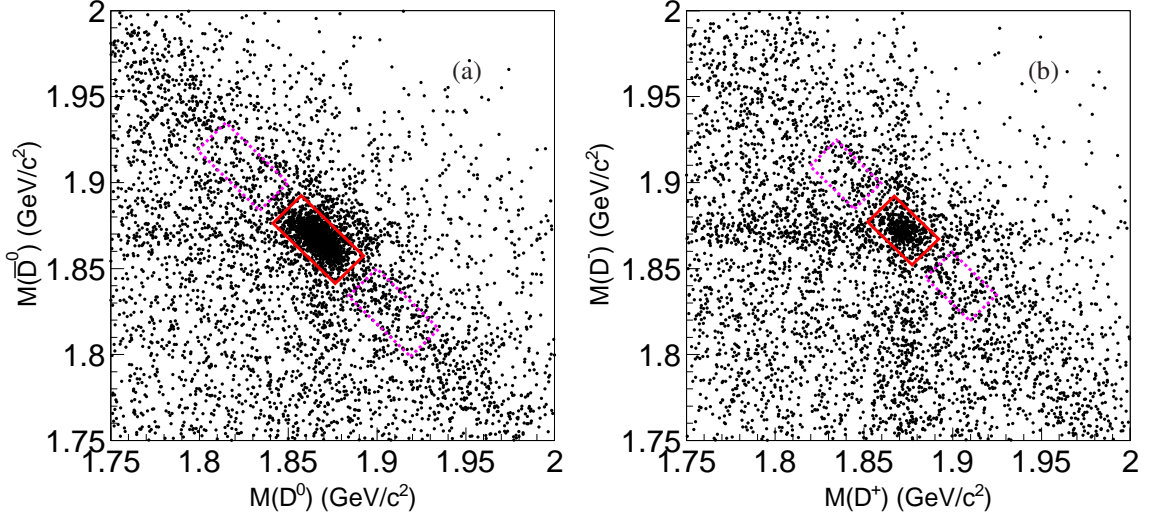


FIG. 1: Scatter plots of the invariant masses of D^0 versus \bar{D}^0 meson candidates (a) and the invariant masses of D^+ versus D^- meson candidates (b) at $\sqrt{s} = 4.42$ GeV. The rectangles show the signal regions (red solid lines) and sideband regions (pink dotted lines).

the BESIII official inclusive MC samples at $\sqrt{s} = 4.23, 4.26, 4.36, 4.42,$ and 4.60 GeV are used. The inclusive MC samples consist of the production of open charm processes, the ISR production of vector charmonium(-like) states, and the continuum processes incorporated in KKMC [34]. The known decay modes are modeled with EVTGEN [36] using branching fractions taken from the Particle Data Group (PDG) [37]. The remaining unknown decays of the charmonium states are generated with LUNDCHARM [38]. The generation of final state radiation (FSR) photons which are produced by charged final state particles is incorporated by the usage of the PHOTOS package [39]. The size of the MC samples is equivalent to the luminosity in data.

In addition, exclusive MC samples with 200,000 events each for the processes $e^+e^- \rightarrow \pi^+\pi^-D^0\bar{D}^0$, $e^+e^- \rightarrow \pi^+\pi^-D^+D^-$, $e^+e^- \rightarrow D^{*+}D^{*-}$ with $D^{*+} \rightarrow D^0\pi^+$ and $D^{*-} \rightarrow \bar{D}^0\pi^-$, $e^+e^- \rightarrow D^{*+}\bar{D}^0\pi^-$ with $D^{*+} \rightarrow D^0\pi^+$, $e^+e^- \rightarrow D_1(2430)^0\bar{D}^0$ with $D_1(2430)^0 \rightarrow D^{*+}\pi^-$, $e^+e^- \rightarrow D_0^*(2400)^0\bar{D}^0$ with $D_0^*(2400)^0 \rightarrow D^+\pi^-$, $e^+e^- \rightarrow D_0^*(2400)^+D^-$ with $D_0^*(2400)^+ \rightarrow D^0\pi^+$ and $e^+e^- \rightarrow D_2^*(2460)^0\bar{D}^0$ with $D_2^*(2460)^0 \rightarrow D^{*+}\pi^-$ are produced at each c.m. energy to study possible background contributions.

III. EVENT SELECTION AND BACKGROUND ANALYSIS

In this analysis the $D\bar{D}$ (denoting $D^0\bar{D}^0$ and D^+D^- in the following) pairs are selected with both D mesons fully reconstructed in a number of hadronic decay channels (also called “double D tag” in the following). D^0 mesons are reconstructed in four decay modes ($K^-\pi^+$, $K^-\pi^+\pi^0$, $K^-\pi^+\pi^+\pi^-$, and $K^-\pi^+\pi^+\pi^-\pi^0$) and D^+ mesons in five decay modes ($K^-\pi^+\pi^+$, $K^-\pi^+\pi^+\pi^0$, $K_S^0\pi^+$, $K_S^0\pi^+\pi^0$,

and $K_S^0\pi^+\pi^-\pi^+$). The \bar{D}^0 and D^- mesons are reconstructed in the charge conjugate final states of the D^0 and D^+ mesons, respectively. One $\pi^+\pi^-$ pair is selected in addition to the tracks from $D\bar{D}$ decays.

Charged tracks are reconstructed from MDC hits within a polar-angle (θ) acceptance range of $|\cos\theta| < 0.93$ and required to pass within 10 cm of the interaction point in the beam direction and within 1 cm in the plane perpendicular to the beam. The TOF and dE/dx information is combined for each charged track to calculate the particle identification (PID) probability P_i ($i = \pi, K$) of each particle-type hypothesis. $P_K > P_\pi$ is required for a kaon candidate and $P_\pi > P_K$ is required for a pion candidate. Tracks used in reconstructing K_S^0 are exempted from these requirements.

Electromagnetic showers are reconstructed by clustering the energy deposits of the EMC crystals. Efficiency and energy resolution are improved by including energy deposits in nearby TOF counters. A photon candidate is defined as a shower with an energy deposit of at least 25 MeV in the “barrel” region ($|\cos\theta| < 0.8$), or at least 50 MeV in the “end-cap” region ($0.86 < |\cos\theta| < 0.92$). Showers in the transition region between the barrel and the end-cap are not well measured and are rejected. An additional requirement on the EMC hit timing ($0 \leq T \leq 700$ ns relative to the event start time) suppresses electronic noise and energy deposits unrelated to the event. To eliminate showers from bremsstrahlung photons which originated from charged particles, the angle between the shower and nearest charged track is required to be greater than 20 degrees.

π^0 candidates are reconstructed from pairs of photon candidates with an invariant mass in the range $0.115 < M_{\gamma\gamma} < 0.150$ GeV/ c^2 . A one-constraint (1C) kinematic fit with the mass of the π^0 constrained to the world average value [37] is performed to improve the energy resolution.

K_S^0 candidates are reconstructed from two oppositely charged tracks which satisfy $|\cos\theta| < 0.93$ for the polar angle and the distance to the average beam position in beam direction within 20 cm. For each pair of tracks, assuming they are π^+ and π^- , a vertex fit is performed and the resulting track parameters are used to obtain the $\pi\pi$ invariant mass which must be in the range $0.487 < M_{\pi\pi} < 0.511$ GeV/ c^2 . The χ^2 from the vertex fit is required to be smaller than 100.

The selected K^\pm , π^\pm , K_S^0 , and π^0 candidates are used to reconstruct D meson candidates which are composed to $D^0\bar{D}^0$ and D^+D^- meson pairs. If more than one $D\bar{D}$ pair per event is found with both D mesons decaying in the same way, the pair with the average mass $\hat{M} = [M(D) + M(\bar{D})]/2$ closest to the nominal mass of the D meson [37] is chosen. In each event, one negative and one positive charged π are required in addition. To reduce the background contribution and improve the mass resolution, a four-constraint (4C) kinematic fit is performed. The total four-momentum of all selected charged tracks and good photons from π^0 are constrained to that of the initial e^+e^- system. If the final state contains a π^0 or K_S^0 meson, its mass is constrained in the kinematic fit as well. If there are multiple candidates in an event, the one with the smallest χ^2 of the kinematic fit is chosen. To find the optimal χ^2 criteria, the figure of merit $\text{FOM} = \frac{n_s}{\sqrt{n_s + n_b}}$ is maximized. Here n_s is the number of signal events from signal MC simulation and n_b is the number of backgrounds events from inclusive MC samples. The χ^2 is required to be less than 56 for the $\pi^+\pi^-D^0\bar{D}^0$ final state with selection efficiency of 90.1% and background rejection rate of 45.5%, and less than 40 for the $\pi^+\pi^-D^+D^-$ final state with selection efficiency of 90.3% and background rejection rate of 29.5%.

In Fig. 1 the invariant mass of D meson candidates is plotted versus that of the \bar{D} meson candidates at $\sqrt{s} = 4.42$ GeV after the selection described above. The signal region indicated by the red line in Fig. 1 is defined as $-6 < \Delta\hat{M} < 10$ MeV/ c^2 and $|\Delta M| < 35$ MeV/ c^2 for $D^0\bar{D}^0$ pairs, and $-5 < \Delta\hat{M} < 10$ MeV/ c^2 and $|\Delta M| < 25$ MeV/ c^2 for D^+D^- pairs, where the $\Delta\hat{M} = \hat{M} - m_D$ and $\Delta M = M(D) - M(\bar{D})$ with m_D being the nominal D meson mass [37]. The sideband regions (indicated by the pink rectangles in Fig. 1) are defined as $-6 < \Delta\hat{M} < 10$ MeV/ c^2 and $50 < |\Delta M| < 120$ MeV/ c^2 for $D^0\bar{D}^0$ pairs, and $-5 < \Delta\hat{M} < 10$ MeV/ c^2 and $40 < |\Delta M| < 90$ MeV/ c^2 for D^+D^- pairs.

In order to suppress the background contribution of $e^+e^- \rightarrow D^{(*)}\bar{D}^{(*)}(\pi)$, we examine if there is a D^* (\bar{D}^*) signal in the $D^0\pi^+$ ($\bar{D}^0\pi^-$) combination. The distributions of $M(D^0\pi^+)$ and $M(\bar{D}^0\pi^-)$ are shown in Fig. 2. To improve the mass resolution, $M(D^0\pi^+)$ is calculated as $M(D^0\pi^+) - M(D^0) + m_{D^0}$ and $M(\bar{D}^0\pi^-)$ as $M(\bar{D}^0\pi^-) - M(\bar{D}^0) + m_{\bar{D}^0}$, thereby eliminating the effect of the mass resolution from the reconstruction of the D^0 (\bar{D}^0) meson. The criteria $M(D^0\pi^+) > 2.017$ GeV/ c^2 and $M(\bar{D}^0\pi^-) > 2.017$ GeV/ c^2 are applied to the processes $e^+e^- \rightarrow \pi^+\pi^-\psi(3770)$, $\psi(3770) \rightarrow D^0\bar{D}^0$, $e^+e^- \rightarrow \rho^0 X_2(4013)$, $X_2(4013) \rightarrow D^0\bar{D}^0$, and $e^+e^- \rightarrow D_1(2420)^0\bar{D}^0, D_1(2420)^0 \rightarrow$

$D^0\pi^+\pi^-$. The criteria $M(D^0\pi^+) < 2.017$ GeV/ c^2 and $M(\bar{D}^0\pi^-) > 2.017$ GeV/ c^2 are applied to the process $e^+e^- \rightarrow D_1(2420)^0\bar{D}^0, D_1(2420)^0 \rightarrow D^{*+}\pi^-$, and the criteria $M(D^0\pi^+) > 2.017$ GeV/ c^2 and $M(\bar{D}^0\pi^-) < 2.017$ GeV/ c^2 are applied to the charged conjugate process.

The inclusive MC sample is used to investigate possible background contributions. There is neither a peaking background contribution found near 3.773 GeV/ c^2 and 4.013 GeV/ c^2 in the $D\bar{D}$ invariant mass distribution nor near 2.42 GeV/ c^2 in the $D\pi\pi$ invariant mass distribution. From the study of the MC samples with highly excited charmed mesons, we find that only the process $e^+e^- \rightarrow D_2^*(2460)^0\bar{D}^0, D_2^*(2460)^0 \rightarrow D^{*+}\pi^-$ produces a peak near 2.46 GeV/ c^2 in the signal region of the $D_1(2420)^0$ in the invariant mass distribution of $D^{*+}\pi^-$. Therefore, $e^+e^- \rightarrow D_2^*(2460)^0\bar{D}^0, D_2^*(2460)^0 \rightarrow D^{*+}\pi^-$ is considered as a component of the background contribution in the study of $e^+e^- \rightarrow D_1(2420)^0\bar{D}^0, D_1(2420)^0 \rightarrow D^{*+}\pi^-$.

There will be some non- $D\bar{D}$ backgrounds remaining in the signal region. According to the study of the inclusive MC, in the $D\bar{D}$ and $D\pi\pi$ invariant mass distribution, non- $D\bar{D}$ backgrounds and sidebands events are consistent with each other. Therefore, the events from the sidebands are used to describe non- $D\bar{D}$ backgrounds in this analysis.

IV. SIGNAL YIELD DETERMINATION

A. $e^+e^- \rightarrow \pi^+\pi^-\psi(3770)$

After imposing all the requirements mentioned above, the $D\bar{D}$ invariant mass distributions are shown in Fig. 3. $M(D\bar{D})$ is used for the expression $M(D\bar{D}) - M(D) - M(\bar{D}) + 2m_D$ to obtain a better mass resolution by eliminating the mass resolution effect coming from the reconstruction of the D and \bar{D} mesons. A peak at around 3.77 GeV/ c^2 can be seen, but there is no evidence for an intermediate state $\psi(1^3D_3)$.

To determine the signal yield of $e^+e^- \rightarrow \pi^+\pi^-\psi(3770)$, an unbinned maximum likelihood fit is performed to the $M(D\bar{D})$ spectra as shown in Fig. 3. The signal contribution is described by the MC simulated shape which is modeled using non-parametric kernel-estimation [40]. The background component includes the channel $D_1(2420)\bar{D}$, the four-body decay $\pi^+\pi^-D\bar{D}$ (both described with the shape taken from the MC simulation which are also modeled with non-parametric kernel-estimation) and the non- $D\bar{D}$ background distribution (described by the $D\bar{D}$ sideband events). In the fit, the signal yields are free parameters with lower limits set to 0. The yields of the $D_1(2420)\bar{D}$ and the $\pi^+\pi^-D\bar{D}$ background contributions are free parameters. The number of non- $D\bar{D}$ background events is fixed to the number of events from the sidebands. The signal yields at $\sqrt{s} = 4.26, 4.36, \text{ and } 4.42$ GeV returned by the fit are $30.7 \pm 9.9, 68.7 \pm 21.8, \text{ and } 99.2 \pm 21.0$ events, respectively. The statistical significance of the signal yield is determined to be $3.2\sigma, 3.3\sigma, \text{ and } 5.2\sigma$, respectively, by comparing the log-likelihood values with and without the

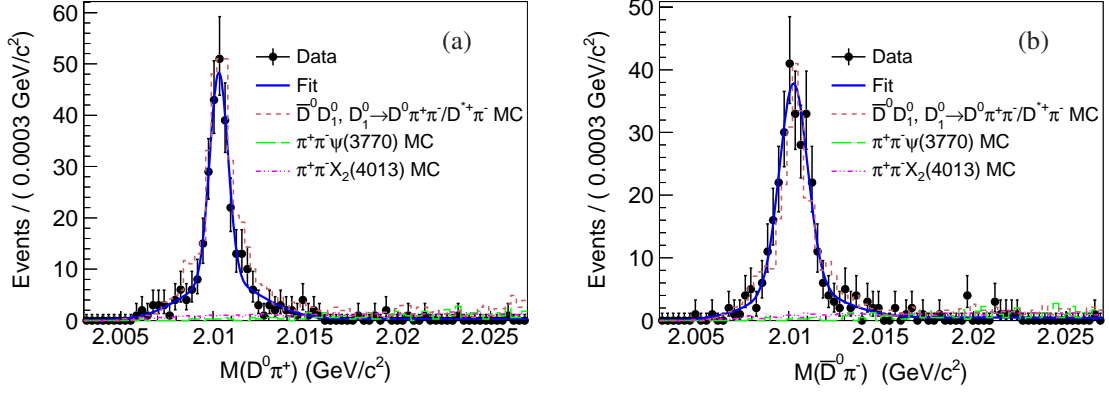


FIG. 2: Distributions of the invariant masses $M(D^0\pi^+)$ (a) and $M(\bar{D}^0\pi^-)$ (b) at $\sqrt{s} = 4.42$ GeV. The black dots with error bars are data and the blue solid lines are the fit results. The brown dashed lines are the distributions from $\bar{D}^0 D_1^0$ and the green long-dashed lines the distributions from $\pi^+\pi^-\psi(3770)$. The pink dotted-dotted-dashed lines show the distribution from $\pi^+\pi^-X_2(4013)$. The distributions from $\bar{D}^0 D_1^0$ are normalized to the maximum bin content of data, and the distributions from $\pi^+\pi^-\psi(3770)$ and $\pi^+\pi^-X_2(4013)$ are normalized arbitrarily.

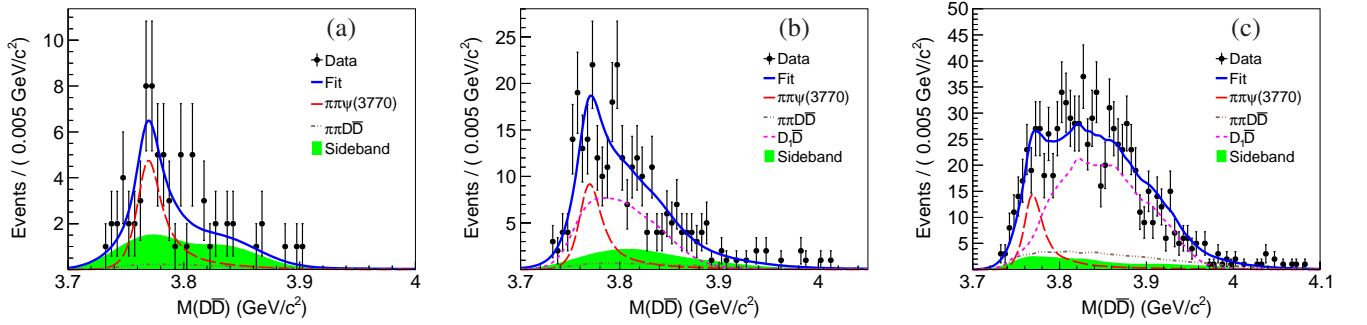


FIG. 3: Fit to the $D\bar{D}$ invariant mass distribution at $\sqrt{s} = 4.26$ (a), 4.36 (b), and 4.42 (c) GeV. The black dots with error bars are data and the blue solid lines are the fit results. The red long-dashed lines indicate the contribution of the $\psi(3770)$ and the pink dashed lines the contribution of the $D_1(2420)\bar{D}$ final state. The brown dotted-dashed lines show the $\pi^+\pi^-D\bar{D}$ background contributions and the green shaded histograms are the distributions from the sideband regions.

signal hypothesis and taking the change in the number of degrees of freedom into account. With the same method, the data samples taken at other c.m. energies are also studied as shown in Fig. 8 of Appendix A. The signal yields are listed in Table I. In this analysis, if the statistical significance of the signal is less than 1σ , we will scan the likelihood distribution as a function of the signal yield greater than 0 and use the difference between the most probable values and the thresholds of 68.3% total integral area as the errors.

We also search for structures in the $\pi^\pm\psi(3770)$ invariant mass distribution at the energy points where the $\pi\pi\psi(3770)$ signal is most prominent. The $\pi^\pm\psi(3770)$ distribution after requiring $M(D\bar{D}) \in [3.73, 3.80]$ GeV/ c^2 around the $\psi(3770)$ mass is shown in Fig. 4. There are hints for peaks at 4.04 and 4.13 GeV/ c^2 in $\sqrt{s} = 4.42$ GeV data, but the statistical significance is low.

B. $e^+e^- \rightarrow \rho^0 X_2(4013)$

For the search for the $X_2(4013)$ resonance, the region of large $D\bar{D}$ invariant masses is investigated. Figure 5 shows the distributions after imposing all the requirements above. There is no obvious signal visible around 4.013 GeV/ c^2 . We try to fit these distributions with the signal shape of the process $\rho^0 X_2(4013)$ taken from the MC simulation and a third order polynomial as background distribution as shown in Fig. 5. The signal yields are $1.1_{-1.1}^{+1.5}$, $0.0_{-0.0}^{+1.8}$ and $2.7_{-2.7}^{+5.3}$ events with the statistical significance of 1.5σ , 0σ , and 0.5σ for the data sets at $\sqrt{s} = 4.36, 4.42$, and 4.60 GeV, respectively. Results are listed in Table II.

C. $e^+e^- \rightarrow D_1(2420)\bar{D}$

After imposing all the requirements above, the $D\pi^+\pi^-$ invariant mass distributions are shown in Fig. 6. A peak at

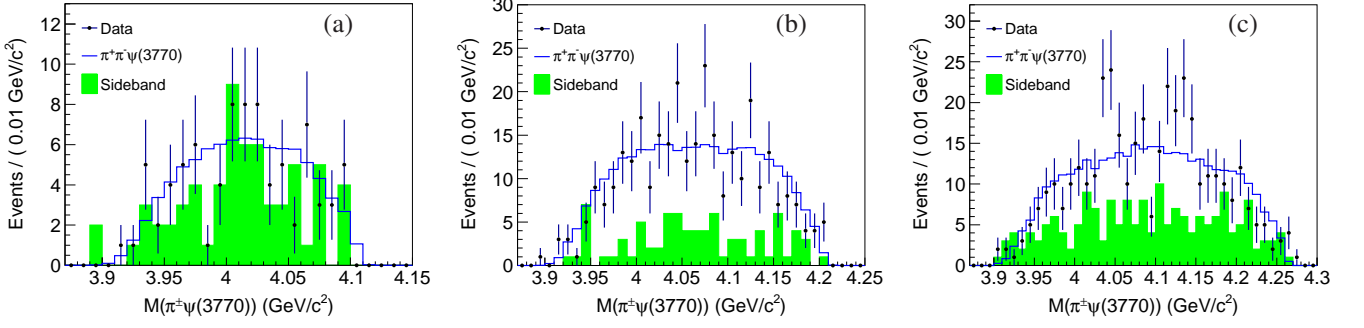


FIG. 4: Distribution of the $M(\pi^+\psi(3770))$ invariant mass at $\sqrt{s} = 4.26$ (a), 4.36 (b), 4.42 (c) GeV. The black dots with error bars are data. The blue histograms show the distributions of the MC simulation of the process $e^+e^- \rightarrow \pi^+\pi^-\psi(3770)$ (phase space distributed), while the green shaded histograms are the distributions from the sideband regions.

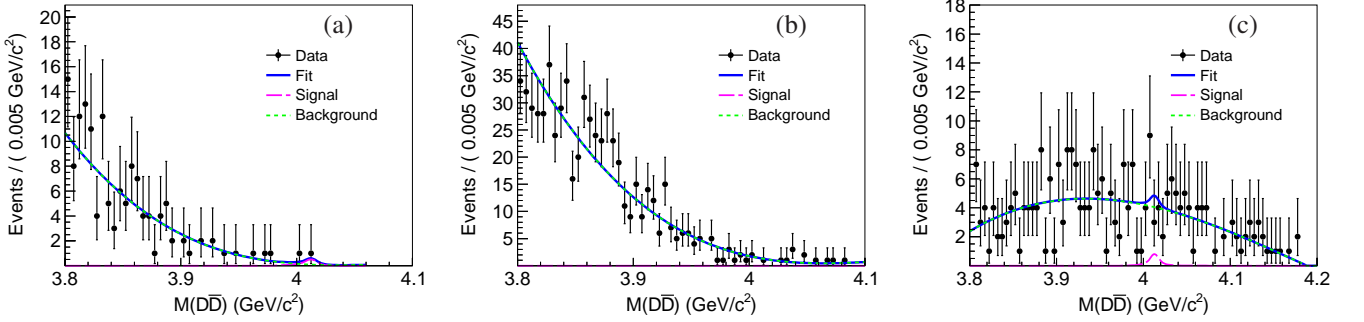


FIG. 5: Fit to the region of large $D\bar{D}$ invariant masses at $\sqrt{s} = 4.36$ (a), 4.42 (b), and 4.60 (c) GeV. The black dots with error bars are data, the blue solid curves are the fit results, the pink long-dashed lines show the X(4013) signal contribution and the green dashed lines describe the background distribution.

around $2.42 \text{ GeV}/c^2$ can be seen.

To determine the signal yield for the reaction $e^+e^- \rightarrow D_1(2420)^0\bar{D}^0$, the $D^0\pi^+\pi^-$ invariant mass distribution is fitted with the signal shape taken from the MC simulation convolved with a Gaussian function to take into account the shift of the reconstructed mass to the generated one and the difference in the mass resolution between data and MC simulation as shown in Fig. 6. As background components, the channels $\pi^+\pi^-\psi(3770)$ and $\pi^+\pi^-D^0\bar{D}^0$ are included in the fit as well as a non- $D\bar{D}$ component, which is fixed to the shape and number of events expected from the sideband regions. The numbers of $\pi^+\pi^-\psi(3770)$ events are fixed to the values calculated using the cross sections we measured (see Table II). The yields of the signal events and of the $\pi^+\pi^-D^0\bar{D}^0$ events are allowed to vary in the fit. The signal yields at $\sqrt{s} = 4.36, 4.42,$ and 4.60 GeV are $114.7 \pm 13.8, 252.3 \pm 39.4,$ and 43.8 ± 15.1 events with a statistical significance of $3.2\sigma, 7.4\sigma,$ and 3.3σ , respectively.

A similar fit is performed to the $D^{*+}\pi^-$ invariant mass distribution as shown in Fig. 6. The signal shape is taken from the MC simulation in the same way as described above. As background components, the channels $D^*\bar{D}\pi$ and $D_2^*(2460)^0\bar{D}$ are included in the fit as well as the non- $D\bar{D}$ component taken from the sideband regions. The signal yields at $\sqrt{s} = 4.36, 4.42,$ and 4.60 GeV are $17.8 \pm 9.3, 22.3 \pm 13.2,$ and 12.6 ± 7.3

events with the statistical significance of $1.6\sigma, 2.4\sigma,$ and 1.5σ , respectively.

To determine the signal yield of $e^+e^- \rightarrow D_1(2420)^+D^-$, the $D^+\pi^+\pi^-$ invariant mass distribution is fitted with a procedure similar to the neutral mode as shown in Fig. 6. The signal yields at $\sqrt{s} = 4.36, 4.42,$ and 4.60 GeV are $68.4 \pm 17.3, 132.8 \pm 31.4,$ and 17.7 ± 10.2 events with the statistical significance of $3.1\sigma, 3.0\sigma,$ and 2.1σ , respectively.

The data samples taken at other c.m. energies are also studied with the same method. The fits are shown in Figs. 9-11 in Appendix B. Signal yields are listed in Tables III-V.

V. CROSS SECTION RESULTS

The Born cross section of $e^+e^- \rightarrow \pi^+\pi^-\psi(3770)$ is calculated with

$$\sigma^B = \frac{N^{\text{obs}}}{\mathcal{L}_{\text{int}} f_r f_v (\mathcal{B}_N \sum_{i,j} \epsilon_{i,j} \mathcal{B}_i \mathcal{B}_j + \mathcal{B}_C \sum_{k,l} \epsilon_{k,l} \mathcal{B}_k \mathcal{B}_l)}, \quad (1)$$

where N^{obs} is the number of observed events, \mathcal{L}_{int} the integrated luminosity and $\epsilon_{i,j}$ the selection efficiency for $e^+e^- \rightarrow \pi^+\pi^-\psi(3770), \psi(3770) \rightarrow D^0\bar{D}^0, D^0 \rightarrow i, \bar{D}^0 \rightarrow j$. \mathcal{B}_N

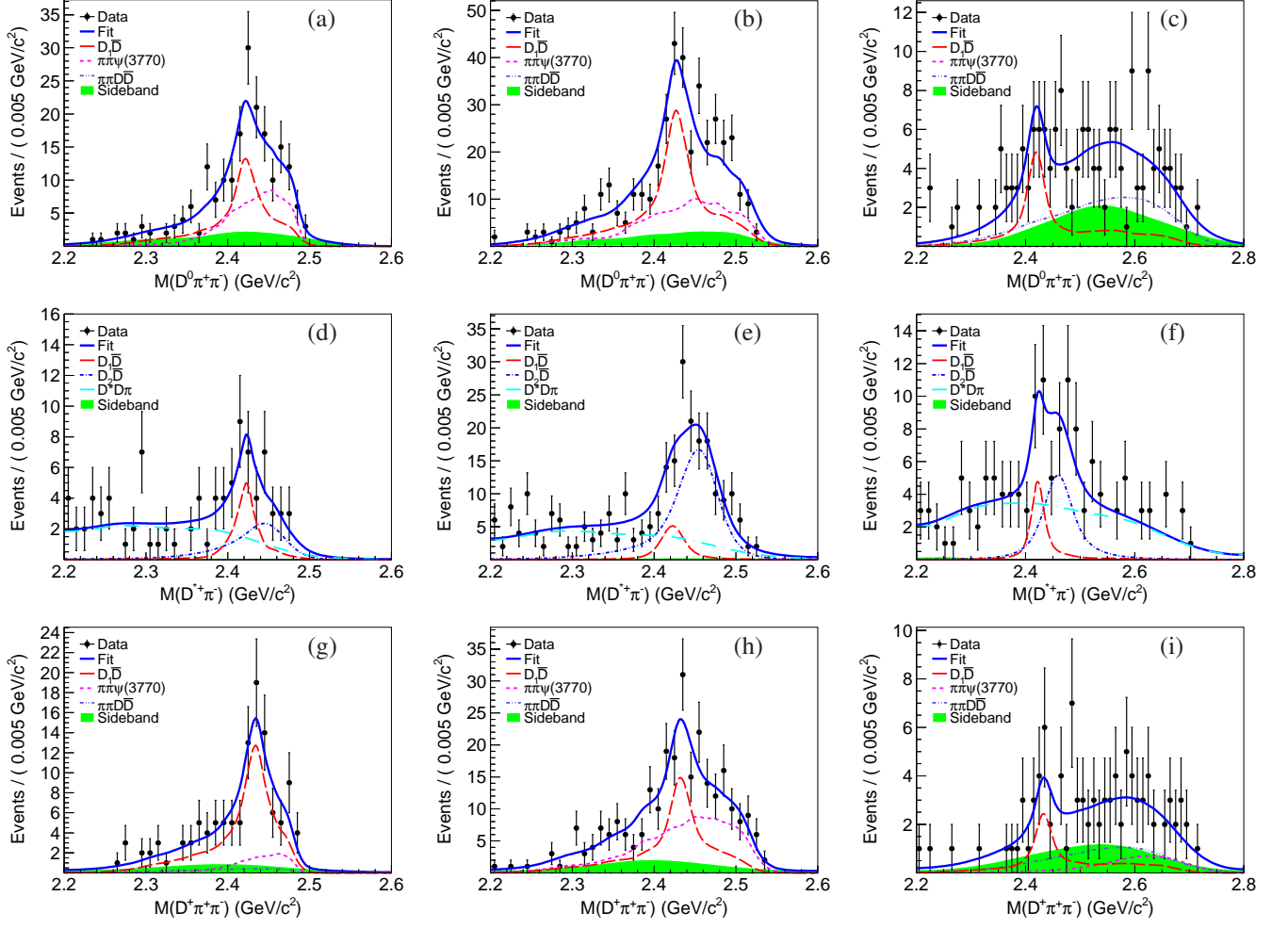


FIG. 6: Fit to the $D^0\pi^+\pi^-$ (first row), $D^{*+}\pi^-$ (second row) and $D^+\pi^+\pi^-$ (third row) invariant mass distribution at $\sqrt{s} = 4.36$ (a, d, g), 4.42 (b, e, h), and 4.60 (c, f, i) GeV. The black dots with error bars are data, the blue solid curves the fit results, and the red long-dashed lines the $D_1(2420)$ signal contributions. The pink dashed lines are the contributions of the final state $\pi^+\pi^-\psi(3770)$, the blue dotted-dashed lines these of the $\pi^+\pi^-D\bar{D}$ or $D_s^{*0}\bar{D}$ final state, and the light blue dotted-long-dashed lines the $D^*\bar{D}\pi$ background contributions, while the green shaded histograms are the distributions from the sideband regions.

and \mathcal{B}_C are the branching fractions for $\psi(3770) \rightarrow D^0\bar{D}^0$ and $\psi(3770) \rightarrow D^+D^-$ and \mathcal{B}_i (\mathcal{B}_j) is the branching fraction for $D^0 \rightarrow i$ ($\bar{D}^0 \rightarrow j$) taken from PDG [37]. The same applies to $\epsilon_{k,l}$ and \mathcal{B}_k (\mathcal{B}_l) for charged mode. $f_v = \frac{1}{|1-\Pi|^2}$ is the vacuum polarization factor [41] and $f_r = (1 + \delta^r)$ is the radiative correction factor which is defined as

$$(1 + \delta^r) = \frac{\sigma^{\text{obs}}}{\sigma^{\text{dressed}}} = \frac{\int \sigma^{\text{dressed}}(s(1-x))F(x,s)dx}{\sigma^{\text{dressed}}(s)}. \quad (2)$$

$F(x,s)$ is the radiator function, which is calculated from QED [42] with an accuracy of 0.1%, $x \equiv 2E_\gamma^*/\sqrt{s} = 1 - m^2/s$, where E_γ^* is the ISR photon energy and m is the invariant mass of the final state after radiating the photon. $\sigma^{\text{dressed}}(s)$ is the energy dependent dressed cross section of $e^+e^- \rightarrow \pi^+\pi^-\psi(3770)$. Here the observed signal events are assumed to originate from the $Y(4260)$ resonance to obtain the efficiency and the ISR correction factor. Then the mea-

sured line shape is used as input to calculate the efficiency and ISR correction factor again. This procedure is repeated until the difference between two subsequent iterations is comparable with the statistical uncertainties. The Born cross sections are listed in Table I and shown in Fig. 7. At the energy points where no significant $\psi(3770)$ signal yields are observed (significance $< 5\sigma$) the upper limits on the cross sections at the 90% confidence level (C.L.) are calculated using the Bayesian method [37] with a flat prior. By fitting the $D\bar{D}$ invariant mass distribution with fixed values for the signal yield, we obtain a scan of the likelihood distribution as a function of the cross section. To take all systematic uncertainties into consideration we convolve the likelihood distribution with a Gaussian function with a width corresponding to the total systematic uncertainty. The upper limit on σ at the 90% C.L. is obtained

TABLE I: Results for the process $e^+e^- \rightarrow \pi^+\pi^-\psi(3770)$. Shown in the table are the number of observed events N^{obs} , the integrated luminosity L_{int} , the radiation correction factor $1 + \delta^r$, the vacuum polarization correction factor $\frac{1}{|1-\Pi|^2}$, the summation over the products of branching fraction and efficiency $\sum_{i,j} \epsilon_{i,j} \mathcal{B}_i \mathcal{B}_j$ (left) for the $D^0 \bar{D}^0$ and (right) for the $D^+ D^-$ mode, the Born cross section σ^B and the statistical significance S. The upper limits are at 90% C.L.

\sqrt{s} (GeV)	N^{obs}	$L_{\text{int}}(\text{pb}^{-1})$	$1 + \delta^r$	$\frac{1}{ 1-\Pi ^2}$	$\sum_{i,j} \epsilon_{i,j} \mathcal{B}_i \mathcal{B}_j$	σ^B (pb)	S
4.0854	$0.0_{-0.0}^{+1.1}$	52.6	0.78	1.052	0.0005 0.0005	$0.0_{-0.0}^{+57.2} \pm 0.0 (<120)$	-
4.1886	$0.0_{-0.0}^{+1.6}$	43.1	0.84	1.056	0.0043 0.0032	$0.0_{-0.0}^{+11.9} \pm 0.0 (<25)$	-
4.2077	$0.0_{-0.0}^{+2.2}$	54.6	0.84	1.057	0.0047 0.0036	$0.0_{-0.0}^{+11.6} \pm 0.0 (<24)$	-
4.2171	$0.0_{-0.0}^{+1.8}$	54.1	0.86	1.057	0.0048 0.0036	$0.0_{-0.0}^{+9.2} \pm 0.0 (<20)$	-
4.2263	14.3 ± 8.6	1047.3	0.81	1.056	0.0049 0.0037	$3.9 \pm 2.4 \pm 0.6 (<7.9)$	1.4σ
4.2417	$0.0_{-0.0}^{+2.0}$	55.6	0.81	1.056	0.0050 0.0038	$0.0_{-0.0}^{+10.1} \pm 0.0 (<21)$	-
4.2580	30.7 ± 9.9	825.7	0.77	1.054	0.0050 0.0038	$11.1 \pm 3.6 \pm 1.7 (<16)$	3.2σ
4.3079	$0.0_{-0.0}^{+2.7}$	44.9	0.90	1.052	0.0047 0.0036	$0.0_{-0.0}^{+16.5} \pm 0.0 (<36)$	-
4.3583	68.7 ± 21.8	539.8	0.95	1.051	0.0039 0.0029	$39.5 \pm 12.5 \pm 5.9 (<59)$	3.3σ
4.3874	14.7 ± 6.6	55.2	0.93	1.051	0.0035 0.0027	$93.3 \pm 41.9 \pm 14.0 (<166)$	2.7σ
4.4156	99.2 ± 21.0	1028.9	0.95	1.053	0.0025 0.0020	$46.0 \pm 9.7 \pm 5.9$	5.2σ
4.4671	$1.5_{-1.5}^{+3.6}$	109.9	0.93	1.055	0.0025 0.0019	$6.6 \pm 16.8 \pm 0.8 (<39)$	0.1σ
4.5271	$0.0_{-0.0}^{+1.4}$	110.0	0.95	1.055	0.0022 0.0017	$0.0_{-0.0}^{+6.8} \pm 0.0 (<18)$	-
4.5745	4.4 ± 2.7	47.7	0.94	1.055	0.0020 0.0016	$54.0 \pm 33.1 \pm 6.9 (<123)$	1.4σ
4.5995	$3.7_{-3.7}^{+7.9}$	566.9	0.96	1.055	0.0019 0.0015	$3.9_{-3.9}^{+8.4} \pm 0.5 (<20)$	0.5σ

TABLE II: Results for the reaction channel $e^+e^- \rightarrow \rho^0 X_2(4013)$. For the symbols see Table I, the penultimate column is the Born cross section σ^B times the branching fraction of $X_2(4013) \rightarrow D\bar{D}$. The upper limits are at 90% C.L.

\sqrt{s} (GeV)	N^{obs}	$L_{\text{int}}(\text{pb}^{-1})$	$1 + \delta^r$	$\frac{1}{ 1-\Pi ^2}$	$\sum_{i,j} \epsilon_{i,j} \mathcal{B}_i \mathcal{B}_j$	$\sigma^B \cdot \mathcal{B}_{X_2(4013) \rightarrow D\bar{D}}$ (pb)	S
4.3583	$1.1_{-1.1}^{+1.5}$	539.8	0.92	1.051	0.0018 0.0017	$1.2_{-1.2}^{+1.6} \pm 0.2 (<4.8)$	1.5σ
4.4156	$0.0_{-0.0}^{+1.8}$	1028.9	0.93	1.053	0.0045 0.0035	$0.0_{-0.0}^{+0.4} \pm 0.0 (<1.0)$	-
4.5995	$2.7_{-2.7}^{+5.3}$	566.9	0.95	1.055	0.0054 0.0042	$1.0_{-1.0}^{+1.9} \pm 0.2 (<5.5)$	0.5σ

TABLE III: Results for the process $e^+e^- \rightarrow D_1(2420)^0 \bar{D}^0$ with $D_1(2420)^0 \rightarrow D^0 \pi^+ \pi^- + c.c.$ For the symbols see Table I, the penultimate column is the Born cross section σ^B times the branching fraction of $D_1(2420)^0 \rightarrow D^0 \pi^+ \pi^-$. The upper limits are at 90% C.L.

\sqrt{s} (GeV)	N^{obs}	$L_{\text{int}}(\text{pb}^{-1})$	$1 + \delta^r$	$\frac{1}{ 1-\Pi ^2}$	$\sum_{i,j} \epsilon_{i,j} \mathcal{B}_i \mathcal{B}_j$	$\sigma^B \cdot \mathcal{B}_{D_1^0 \rightarrow D^0 \pi^+ \pi^-}$ (pb)	S
4.3079	2.4 ± 1.7	44.9	0.87	1.052	0.0049	$11.8 \pm 8.4 \pm 2.4 (<31)$	1.4σ
4.3583	114.7 ± 13.8	539.8	0.94	1.051	0.0041	$52.2 \pm 6.3 \pm 9.8 (<66)$	3.2σ
4.3874	15.5 ± 10.8	55.2	0.95	1.051	0.0037	$76.6 \pm 53.4 \pm 14.4 (<142)$	1.3σ
4.4156	252.3 ± 39.4	1028.9	0.94	1.053	0.0028	$89.5 \pm 14.0 \pm 12.8$	7.4σ
4.4671	6.9 ± 5.6	109.9	0.92	1.055	0.0028	$23.3 \pm 18.9 \pm 3.3 (<52)$	1.5σ
4.5271	5.6 ± 2.9	110.0	0.94	1.055	0.0024	$21.3 \pm 11.0 \pm 3.6 (<44)$	1.3σ
4.5745	$2.8_{-2.8}^{+2.3}$	47.7	0.94	1.055	0.0023	$25.7_{-25.7}^{+21.1} \pm 4.4 (<80)$	0.7σ
4.5995	43.8 ± 15.1	566.9	0.95	1.055	0.0022	$35.0 \pm 12.1 \pm 5.9 (<56)$	3.3σ

from

$$\int_0^\sigma L(x) dx / \int_0^\infty L(x) dx = 0.9. \quad (3)$$

All upper limits on the cross sections are also listed in Table I.

For the reaction channel $e^+e^- \rightarrow \rho^0 X_2(4013)$ the

upper limit of the product of the Born cross section and the branching fraction to $D\bar{D}$ is measured, assuming $\mathcal{B}_{X_2(4013) \rightarrow D^0 \bar{D}^0} = \mathcal{B}_{X_2(4013) \rightarrow D^+ D^-} = 0.5 \times \mathcal{B}_{X_2(4013) \rightarrow D\bar{D}}$. The efficiency and ISR correction factor in Eq. (1) is taken from the MC sample with the $X_2(4013)$ resonance as intermediate state and the cross-section following the $Y(4260)$ line shape. The upper limits on the cross sections at

TABLE IV: Results for the reaction channel $e^+e^- \rightarrow D_1(2420)^0 \bar{D}^0$ with $D_1(2420)^0 \rightarrow D^{*+}\pi^- + c.c.$ (For symbols see Table III).

$\sqrt{s}(\text{GeV})$	N^{obs}	$L_{int}(\text{pb}^{-1})$	$1 + \delta^r$	$\frac{1}{ 1-\Pi ^2}$	$\sum_{i,j} \epsilon_{i,j} \mathcal{B}_i \mathcal{B}_j$	$\sigma^B \cdot \mathcal{B}_{D_1^0 \rightarrow D^{*+}\pi^-}(\text{pb})$	S
4.3079	$1.8^{+1.6}_{-1.8}$	44.9	0.92	1.052	0.00052	$80.1^{+71.2}_{-80.1} \pm 13.8 (<231)$	0.8σ
4.3583	17.8 ± 9.3	539.8	0.92	1.051	0.00059	$57.7 \pm 30.2 \pm 9.3 (<107)$	1.6σ
4.3874	$0.4^{+3.0}_{-0.4}$	55.2	0.94	1.051	0.00061	$12.0^{+90.2}_{-12.0} \pm 1.9 (<210)$	0.5σ
4.4156	22.3 ± 13.2	1028.9	0.93	1.053	0.00055	$40.0 \pm 23.7 \pm 6.0 (<78)$	2.4σ
4.4671	$5.1^{+3.0}_{-5.1}$	109.9	0.92	1.055	0.00059	$80.5^{+47.4}_{-80.5} \pm 12.1 (<194)$	0.9σ
4.5271	$0.0^{+2.2}_{-0.0}$	110.0	0.94	1.055	0.00062	$0.0^{+32.6}_{-0.0} \pm 0.0 (<71)$	-
4.5745	$0.5^{+2.0}_{-0.5}$	47.7	0.94	1.055	0.00064	$16.4^{+70.0}_{-16.4} \pm 2.9 (<174)$	0.1σ
4.5995	12.6 ± 7.3	566.9	0.95	1.055	0.00065	$34.4 \pm 19.9 \pm 6.0 (<70)$	1.5σ

TABLE V: Results for the reaction channel $e^+e^- \rightarrow D_1(2420)^+ D^-$ with $D_1(2420)^+ \rightarrow D^+ \pi^+ \pi^- + c.c.$ (For symbols see Table III).

$\sqrt{s}(\text{GeV})$	N^{obs}	$L_{int}(\text{pb}^{-1})$	$1 + \delta^r$	$\frac{1}{ 1-\Pi ^2}$	$\sum_{i,j} \epsilon_{i,j} \mathcal{B}_i \mathcal{B}_j$	$\sigma^B \cdot \mathcal{B}_{D_1^+ \rightarrow D^+ \pi^+ \pi^-}(\text{pb})$	S
4.3079	$0.0^{+2.2}_{-0.0}$	44.9	0.88	1.052	0.0041	$0.0^{+13.0}_{-0.0} \pm 0.0 (<26)$	-
4.3583	68.4 ± 17.3	539.8	0.95	1.051	0.0032	$39.7 \pm 10.0 \pm 7.6 (<54)$	3.1σ
4.3874	$1.4^{+3.5}_{-1.4}$	55.2	0.94	1.051	0.0031	$8.3^{+20.2}_{-8.3} \pm 1.6 (<49)$	-
4.4156	132.8 ± 31.4	1028.9	0.94	1.053	0.0024	$54.0 \pm 12.8 \pm 7.6 (<76)$	3.0σ
4.4671	9.5 ± 6.8	109.9	0.92	1.055	0.0023	$38.8 \pm 27.8 \pm 5.4 (<72)$	1.7σ
4.5271	2.3 ± 1.9	110.0	0.94	1.055	0.0020	$10.3 \pm 8.5 \pm 1.6 (<29)$	1.0σ
4.5745	4.8 ± 2.7	47.7	0.94	1.055	0.0020	$51.4 \pm 28.9 \pm 8.0 (<110)$	2.0σ
4.5995	17.7 ± 10.2	566.9	0.94	1.055	0.0017	$18.9 \pm 10.9 \pm 2.9 (<36)$	2.1σ

90% C.L. are estimated using the same method as described above. All results and upper limits are listed in Table II.

For the reaction channel $e^+e^- \rightarrow D_1(2420)\bar{D}$ with $D_1(2420) \rightarrow X(D\pi^+\pi^- \text{ or } D^*\pi)$, the product of the Born cross section times the branching fraction of $D_1(2420) \rightarrow X$ is calculated using

$$\sigma^B \times \mathcal{B}_{D_1(2420) \rightarrow X} = \frac{N^{obs}}{\mathcal{L}_{int} f_v f_r \sum_{i,j} \epsilon_{i,j} \mathcal{B}_i \mathcal{B}_j}, \quad (4)$$

where $\epsilon_{i,j}$ is the selection efficiency for each process $e^+e^- \rightarrow D_1(2420)\bar{D}$ ($D_1(2420) \rightarrow D\pi\pi/D^*\pi$, $D \rightarrow i$, $\bar{D} \rightarrow j$). The low momentum of the π meson from $D^* \rightarrow D\pi$ decay reduces the efficiency for the decay channel $D_1(2420) \rightarrow D^*\pi$ in comparison to $D_1(2420) \rightarrow D\pi\pi$. The other variables are the same as defined in Eq. (1). For the $D_1(2420) \rightarrow D^*\pi$ channel, the branching fraction $\mathcal{B}_{D^* \rightarrow D\pi}$ is taken into account. The cross sections as a function of c.m. energy are shown in Fig. 7. At the energy points where no significant D_1 signals are observed (significance $< 5\sigma$), the upper limits on the cross sections at the 90% C.L. are estimated using the same method as described above. All numbers are shown in the Tables III, IV, and V for the neutral and the charged modes, respectively.

VI. SYSTEMATIC UNCERTAINTY ESTIMATION

The systematic uncertainties in the cross section measurements mainly stem from the integrated luminosity, the tracking and photon detection efficiency, various intermediate branching fractions, the ISR correction factor, the signal and background shapes, the fit range, the signal region of double tag of the D mesons, and the cross section of the $\pi^+\pi^-\psi(3770)$ final state. The estimation of the systematic uncertainties is described in the following and the results at $\sqrt{s} = 4.36, 4.42, \text{ and } 4.60$ GeV are listed in Tables VI-X. The results for all other energy points are listed in Appendix C.

TABLE VI: Relative systematic uncertainties (in %) on the $\sigma(e^+e^- \rightarrow \pi^+\pi^-\psi(3770))$ measurement.

Sources / $\sqrt{s}(\text{GeV})$	4.3583	4.4156	4.5995
Integrated luminosity	1.0	1.0	1.0
Efficiency related	8.9	8.8	8.6
Radiative correction	0.6	2.1	0.2
Signal shape	3.4	3.8	3.8
Background shape	9.9	7.6	7.6
Fit range	2.0	2.4	2.4
Signal region of double tag	5.3	2.0	2.0
Total	14.9	12.8	12.5

(a) The uncertainty from the integrated luminosity measurement using Bhabha ($e^+e^- \rightarrow e^+e^-$) scattering events is esti-

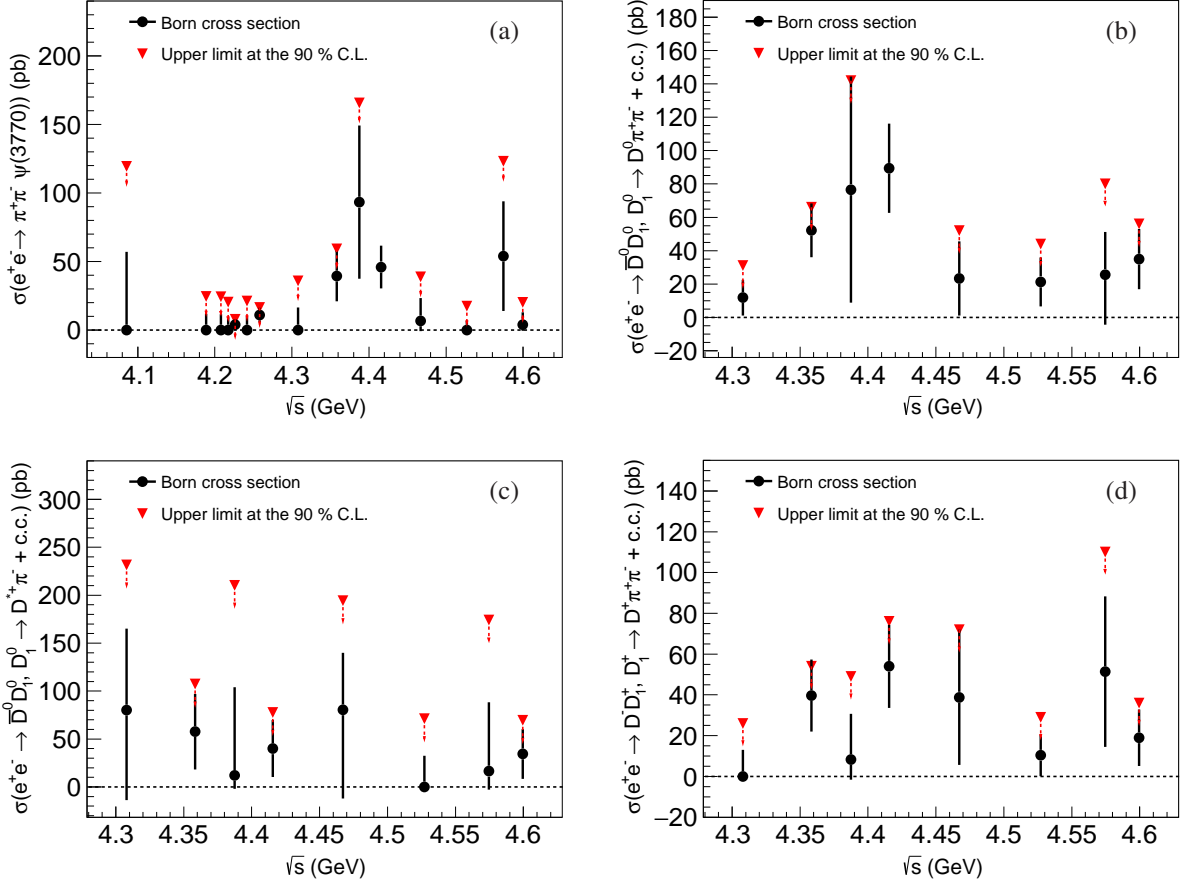


FIG. 7: Born cross sections of the processes (black dots) $e^+e^- \rightarrow \pi^+\pi^-\psi(3770)$ (a), $e^+e^- \rightarrow D_1(2420)^0\bar{D}^0 \rightarrow \pi^+\pi^-D^0\bar{D}^0$ (b), $e^+e^- \rightarrow D_1(2420)^0\bar{D}^0 \rightarrow D^{*+}\bar{D}^0\pi^- \rightarrow \pi^+\pi^-D^0\bar{D}^0$ (c), and $e^+e^- \rightarrow D_1(2420)^+D^- \rightarrow \pi^+\pi^-D^+D^-$ (d). The error bars include the statistical and systematic uncertainties. The red triangles are the upper limits on the Born cross sections at the 90 % C.L.

TABLE VII: Relative systematic uncertainties (in %) on the $\sigma(e^+e^- \rightarrow \rho^0 X_2(4013) \rightarrow \pi^+\pi^-DD)$ measurement.

Sources / \sqrt{s} (GeV)	4.3583	4.4156	4.5995
Integrated luminosity	1.0	1.0	1.0
Efficiency related	9.0	9.0	9.0
Radiative correction	5.6	14.5	5.9
Signal shape	9.9	0.0	11.5
Background shape	3.2	0.0	4.6
Fit range	4.5	0.0	4.4
Signal region of double tag	3.3	0.0	12.1
Total	15.9	17.1	20.9

ated to be 1.0% [32].

(b) The systematic uncertainty from the efficiency includes the uncertainties from MC statistics, particle identification, charged track, photon, π^0 , and K_S^0 reconstruction, as well as the branching fractions of the various D decays. The reconstruction uncertainty for each charged track is 1% [43]. The uncertainty from the photon reconstruction is 1% per photon [44], and the uncertainty from the π^0 reconstruction is

TABLE VIII: Relative systematic uncertainties (in %) on the $\sigma(e^+e^- \rightarrow D_1(2420)^0\bar{D}^0, D_1(2420)^0 \rightarrow D^0\pi^+\pi^- + c.c.)$ measurement.

Sources / \sqrt{s} (GeV)	4.3583	4.4156	4.5995
Integrated luminosity	1.0	1.0	1.0
Efficiency related	4.9	5.0	4.9
Radiative correction	0.6	2.1	0.2
Signal shape	7.2	5.5	8.2
Background shape	3.2	1.2	7.4
Fit range	0.9	1.0	0.9
Signal region of double tag	2.6	4.2	4.8
$\sigma(\pi\pi\psi(3770))$	11.4	0.5	1.1
Total	18.8	14.3	17.0

1% per π^0 [44]. The uncertainty from the K_S^0 reconstruction is 4% per K_S^0 [45]. The uncertainty from the particle identification is 1% per track [43]. The systematic uncertainty for the branching fraction $\mathcal{B}(D^{*+} \rightarrow D^0\pi^+)$ is 0.74%. Those for $\mathcal{B}(D^0 \rightarrow K^-\pi^+)$, $\mathcal{B}(D^0 \rightarrow K^-\pi^+\pi^0)$, $\mathcal{B}(D^0 \rightarrow K^-\pi^+\pi^+\pi^-)$, and $\mathcal{B}(D^0 \rightarrow K^-\pi^+\pi^+\pi^-\pi^0)$ are 1.02%, 5.60%, 2.85%, and 9.52%, respectively, and those for

TABLE IX: Relative systematic uncertainties (in %) on the $\sigma(e^+e^- \rightarrow D_1(2420)^0 \bar{D}^0, D_1(2420)^0 \rightarrow D^{*+}\pi^- + c.c.)$ measurement.

Sources / \sqrt{s} (GeV)	4.3583	4.4156	4.5995
Integrated luminosity	1.0	1.0	1.0
Efficiency related	4.9	5.0	4.9
Radiative correction	0.6	2.1	0.2
Signal shape	5.3	2.8	4.9
Background shape	0.2	1.8	0.1
Fit range	2.7	3.9	0.8
Signal region of double tag	4.9	2.6	9.8
Total	16.0	15.1	17.5

TABLE X: Relative systematic uncertainties (in %) on the $\sigma(e^+e^- \rightarrow D_1(2420)^+ D^-, D_1(2420)^+ \rightarrow D^+ \pi^+ \pi^- + c.c.)$ measurement.

Sources / \sqrt{s} (GeV)	4.3583	4.4156	4.5995
Integrated luminosity	1.0	1.0	1.0
Efficiency related	13.4	13.2	13.0
Radiative correction	0.2	1.0	1.5
Signal shape	7.4	4.2	4.1
Background shape	1.6	0.8	3.8
Fit range	1.7	0.9	1.7
Signal region of double tag	1.1	1.3	5.2
$\sigma(\pi\pi\psi(3770))$	11.1	0.3	1.7
Total	19.1	14.0	15.4

$\mathcal{B}(D^+ \rightarrow K^- \pi^+ \pi^+)$, $\mathcal{B}(D^+ \rightarrow K^- \pi^+ \pi^+ \pi^0)$, $\mathcal{B}(D^+ \rightarrow K_S^0 \pi^+)$, $\mathcal{B}(D^+ \rightarrow K_S^0 \pi^+ \pi^0)$, $\mathcal{B}(D^+ \rightarrow K_S^0 \pi^+ \pi^- \pi^+)$ are 2.54%, 2.61%, 3.92%, 2.35%, and 2.95%, respectively [37]. The total efficiency related systematic uncertainty is the sum of all these individual uncertainties in quadrature.

(c) ISR photons are simulated by using the KKMC package. The shape of the c.m. energy dependent cross section affects the radiative correction factor and the reconstruction efficiency. For the reactions $e^+e^- \rightarrow \pi^+ \pi^- \psi(3770)$ and $e^+e^- \rightarrow D_1(2420) \bar{D}$, the difference between the last two iterations is taken as the systematic uncertainty. Since we have no knowledge on the production cross section for the reaction $e^+e^- \rightarrow \rho^0 X_2(4013)$, we assume that the cross section of $\rho^0 X_2(4013)$ follows the $Y(4260)$ or the $\psi(4415)$ line shape. The difference between these two assumptions is taken as the systematic uncertainty.

(d) For the determination of the systematic uncertainty caused by the signal shape, additional MC samples are produced by varying the width of the signal resonance by one standard deviation of its world average value [37]. The largest difference of the cross section compared with the nominal value is taken as the systematic uncertainty of the signal shape.

(e) The systematic uncertainty caused by the background shape, which is taken from MC simulation of the final states $\pi^+ \pi^- \psi(3770)$, $D_1(2420) \bar{D}$ and $D_1(2460) \bar{D}$, is estimated by generating alternative MC samples where the width of the $\psi(3770)$, $D_1(2420)$ and $D_1(2460)$ resonances is changed by

one standard deviation of the world average value [37]. The largest difference of the cross section compared with the nominal fit value is taken as the systematic uncertainty of the background shape. The systematic uncertainty originating from the sideband selection is estimated by changing the sideband windows by 10 MeV/ c^2 . The largest difference of the cross section compared with the nominal mass window is taken as systematic uncertainty. For $e^+e^- \rightarrow \rho^0 X_2(4013)$, the background shape is changed from a third order polynomial to a fourth order polynomial, and the difference is taken as the systematic uncertainty of background shape.

(f) The systematic uncertainty caused by the choice of the fit range is estimated by varying the limits of the fit range by 20 MeV/ c^2 . The largest difference of the cross section from the nominal value is taken as systematic uncertainty.

(g) In order to estimate the systematic uncertainty due to the selection of the signal window for the double D -tag method, the whole analysis is repeated by changing the signal region from $|\Delta M| < 35$ MeV/ c^2 , $-6 < \Delta \hat{M} < 10$ MeV/ c^2 to $|\Delta M| < 39$ MeV/ c^2 , $-8 < \Delta \hat{M} < 12$ MeV/ c^2 for the $D^0 \bar{D}^0$ mode and from $|\Delta M| < 25$ MeV/ c^2 , $-5 < \Delta \hat{M} < 10$ MeV/ c^2 to $|\Delta M| < 29$ MeV/ c^2 , $-7 < \Delta \hat{M} < 12$ MeV/ c^2 for the $D^+ D^-$ mode. The difference of the cross section from the nominal value is taken as systematic uncertainty.

(h) The systematic uncertainty caused by the fixed number of $\pi^+ \pi^- \psi(3770)$ events in the fit of $M(D\pi^+\pi^-)$ is estimated by varying the fixed number by one standard deviation. The largest deviation from the nominal cross section is taken as systematic uncertainty.

Tables VI to X summarize all the systematic uncertainties. The overall systematic uncertainty for each process and c.m. energy is obtained by summing up all sources of systematic uncertainties in quadrature, assuming they are uncorrelated.

VII. SUMMARY AND DISCUSSION

In this analysis, the processes $e^+e^- \rightarrow \pi^+ \pi^- D \bar{D}$ are studied by using the data samples collected at $\sqrt{s} = 4.09, 4.19, 4.21, 4.22, 4.23, 4.245, 4.26, 4.31, 4.36, 4.39, 4.42, 4.47, 4.53, 4.575, \text{ and } 4.60$ GeV.

We observe the process $e^+e^- \rightarrow \pi^+ \pi^- \psi(3770)$ for the first time with a statistical significance of 5.2σ at $\sqrt{s} = 4.42$ GeV and see evidence for this process with a statistical significance of 3.2σ and 3.3σ at $\sqrt{s} = 4.26$ and 4.36 GeV, respectively. However, no evidence for the $\psi(1^3D_3)$ state is found. The Born cross section of $e^+e^- \rightarrow \pi^+ \pi^- \psi(3770)$ is measured as shown in Fig. 7. It can be compared with the cross section of the process $e^+e^- \rightarrow \pi^+ \pi^- \psi(1^3D_2)$ [17]. If we take $\mathcal{B}(\psi(1^3D_2) \rightarrow \gamma \chi_{c1}) \approx \frac{250 \text{ keV}}{390 \text{ keV}} \approx 0.64$ [46], the Born cross section of $e^+e^- \rightarrow \pi^+ \pi^- \psi(1^3D_1)$ is an order of magnitude larger than that of $e^+e^- \rightarrow \pi^+ \pi^- \psi(1^3D_2)$ at the same c.m. energies [17]. The $e^+e^- \rightarrow \pi^+ \pi^- \psi(3770)$ line shape looks similar to that of $e^+e^- \rightarrow \pi^+ \pi^- \psi(1^3D_2)$ [17].

Whether the events are from the $Y(4390)$ or the $\psi(4415)$ resonance or from any other resonance cannot be distinguished based on the current statistics. For the data points with enough statistics for the $e^+e^- \rightarrow \pi^+\pi^-\psi(3770)$ final state, no significant structure (*i.e.* a possible Z_c state) is observed in the $\pi^\pm\psi(3770)$ system.

We also search for the state $X_2(4013)$, the proposed heavy-quark-spin-symmetry partner of the $X(3872)$, by analyzing the process $e^+e^- \rightarrow \rho^0 X_2(4013)$ with $X_2(4013) \rightarrow D\bar{D}$. No significant signal for the $X_2(4013)$ is observed in any data sample. The upper limit (at the 90% C.L.) of $\sigma(e^+e^- \rightarrow \rho^0 X_2(4013)) \cdot \mathcal{B}(X_2(4013) \rightarrow D\bar{D})$ is estimated as 5.0, 1.0, and 5.1 pb at $\sqrt{s} = 4.36, 4.42,$ and 4.60 GeV, respectively.

The process $e^+e^- \rightarrow D_1(2420)^0\bar{D}^0, D_1(2420)^0 \rightarrow D^0\pi^+\pi^-$ is observed for the first time with a statistical significance of 7.4σ at $\sqrt{s} = 4.42$ GeV, and we see evidence for this process with statistical significance of 3.2σ and 3.3σ at $\sqrt{s} = 4.36$ and 4.60 GeV, respectively. There is also evidence for the process $e^+e^- \rightarrow D_1(2420)^+D^-, D_1(2420)^+ \rightarrow D^+\pi^+\pi^-$ with statistical significance of 3.1σ and 3.0σ at $\sqrt{s} = 4.36$ and 4.42 GeV, respectively. There is no evidence for the process $e^+e^- \rightarrow D_1(2420)^0\bar{D}^0, D_1(2420)^0 \rightarrow D^{*+}\pi^-$. The Born cross sections of $e^+e^- \rightarrow D_1(2420)^0\bar{D}^0, D_1(2420)^0 \rightarrow D^0\pi^+\pi^-/D_1(2420)^0 \rightarrow D^{*+}\pi^-$ and $e^+e^- \rightarrow D_1(2420)^+D^-, D_1(2420)^+ \rightarrow D^+\pi^+\pi^-$ are measured at $\sqrt{s} = 4.31, 4.36, 4.39, 4.42, 4.47, 4.53, 4.575,$ and 4.60 GeV as shown in Fig. 7. No fast rise of the cross section above the $D_1(2420)\bar{D}$ threshold is visible as indicated in Ref. [28], whose point is also disfavored by Ref. [47]. There is no other obvious structure visible either.

Acknowledgments

The BESIII collaboration thanks the staff of BEPCII and the IHEP computing center for their strong support. This work is supported in part by National Key Basic Research Program of China under Contract No. 2015CB856700; National Natural Science Foundation of China (NSFC) under Contracts Nos. 11625523, 11635010, 11735014; National Natural Science Foundation of China (NSFC) under Contract No. 11835012; the Chinese Academy of Sciences (CAS) Large-Scale Scientific Facility Program; Joint Large-Scale Scientific Facility Funds of the NSFC and CAS under Contracts Nos. U1532257, U1532258, U1732263, U1832207; CAS Key Research Program of Frontier Sciences under Contracts Nos. QYZDJ-SSW-SLH003, QYZDJ-SSW-SLH040; 100 Talents Program of CAS; INPAC and Shanghai Key Laboratory for Particle Physics and Cosmology; German Research Foundation DFG under Contract No. Collaborative Research Center CRC 1044; Istituto Nazionale di Fisica Nucleare, Italy; Koninklijke Nederlandse Akademie van Wetenschappen (KNAW) under Contract No. 530-4CDP03; Ministry of Development of Turkey under Contract No. DPT2006K-120470; National Science and Technology fund; The Knut and Alice Wallenberg Foundation (Sweden) under Contract No. 2016.0157; The Swedish Research Council; U. S. Department of Energy under Contracts Nos. DE-FG02-05ER41374, DE-SC-0010118, DE-SC-0012069; University of Groningen (RuG) and the Helmholtzzentrum fuer Schwerionenforschung GmbH (GSI), Darmstadt.

-
- [1] E. Eichten *et al.*, Phys. Rev. Lett. **34**, 369 (1976).
 [2] Stephen Godfrey and Nathan Isgur, Phys. Rev. D **32**, 189 (1985).
 [3] E. Eichten *et al.*, Phys. Rev. D **17**, 3090 (1978).
 [4] N. Brambilla *et al.*, Eur. Phys. J. C **74**, 2981 (2014).
 [5] A. J. Bevan *et al.* (BaBar and Belle Collaborations), Eur. Phys. J. C **74**, 3026 (2014).
 [6] C. Z. Yuan, Int. J. Mod. Phys. A **33**, no. 21, 1830018 (2018).
 [7] N. Brambilla *et al.*, Eur. Phys. J. C **71**, 1534 (2011).
 [8] H. X. Chen, W. Chen, X. Liu and S. L. Zhu, Phys. Rept. **639**, 1 (2016).
 [9] B. Aubert *et al.* (BABAR Collaboration), Phys. Rev. Lett. **95**, 142001 (2005).
 [10] J. P. Lees *et al.* (BABAR Collaboration), Phys. Rev. D **89**, 111103(R) (2014).
 [11] C. Z. Yuan *et al.* (Belle Collaboration), Phys. Rev. Lett. **99**, 182004 (2007); Z. Q. Liu *et al.* (Belle Collaboration), Phys. Rev. Lett. **110**, 252002 (2013).
 [12] X. L. Wang *et al.* (Belle Collaboration), Phys. Rev. Lett. **99**, 142002 (2007); X. L. Wang *et al.* (Belle Collaboration), Phys. Rev. D **91**, 112007 (2015).
 [13] M. Ablikim *et al.* (BESIII Collaboration), Phys. Rev. Lett. **118**, 092001 (2017).
 [14] M. Ablikim *et al.* (BESIII Collaboration), Phys. Rev. Lett. **110**, 252001 (2013).
 [15] M. Ablikim *et al.* (BESIII Collaboration), Phys. Rev. D **96**, 032004 (2017).
 [16] T. Xiao, S. Dobbs, A. Tomaradze and K. K. Seth, Phys. Lett. B **727**, 366 (2013).
 [17] M. Ablikim *et al.* (BESIII Collaboration), Phys. Rev. Lett. **115**, 011803 (2015).
 [18] T. Barnes, S. Godfrey, and E. S. Swanson, Phys. Rev. D **72**, 054026 (2005).
 [19] S. K. Choi *et al.* (Belle Collaboration), Phys. Rev. Lett. **91**, 262001 (2003).
 [20] D. Acosta *et al.* (CDF Collaboration), Phys. Rev. Lett. **93**, 072001 (2004).
 [21] V. M. Abazov *et al.* (D0 Collaboration), Phys. Rev. Lett. **93**, 162002 (2004).
 [22] B. Aubert *et al.* (BABAR Collaboration), Phys. Rev. D **71**, 071103 (2005).
 [23] N. A. Tornqvist, Phys. Lett. B **590**, 209 (2004).
 [24] E. S. Swanson, Phys. Lett. B **588**, 189 (2004).
 [25] J. Nieves and M. Pavon Valderrama, Phys. Rev. D **86**, 056004 (2012).
 [26] C. Hidalgo-Duque, J. Nieves and M. Pavon Valderrama, Phys. Rev. D **87**, 076006 (2013).
 [27] M. Albaladejo *et al.*, Eur. Phys. J. C **75**, 547 (2015).
 [28] Q. Wang, C. Hanhart and Q. Zhao, Phys. Rev. Lett. **111**, 132003 (2013).
 [29] M. Ablikim *et al.* (BESIII Collaboration), Nucl. Instrum. Meth. A **614**, 345 (2010).

- [30] C. H. Yu *et al.*, Proceedings of IPAC2016, Busan, Korea, 2016, doi:10.18429/JACoW-IPAC2016-TUYA01.
- [31] M. Ablikim *et al.* (BESIII Collaboration), Chin. Phys. C **40**, 063001 (2016).
- [32] M. Ablikim *et al.* (BESIII Collaboration), Chin. Phys. C **39**, 093001 (2015).
- [33] S. Agostinelli *et al.* (GEANT4 Collaboration), Nucl. Instrum. Meth. A **506**, 250 (2003).
- [34] S. Jadach, B. F. L. Ward and Z. Was, Phys. Rev. D **63**, 113009 (2001); Comput. Phys. Commun. **130**, 260 (2000).
- [35] K. Abe *et al.* (Belle Collaboration), Phys. Rev. Lett. **94**, 221805 (2005).
- [36] D. J. Lange, Nucl. Instrum. Meth. A **462**, 152 (2001); R. G. Ping, Chin. Phys. C **32**, 599 (2008).
- [37] M. Tanabashi *et al.* (Particle Data Group), Phys. Rev. D **98**, 030001 (2018).
- [38] J. C. Chen, G. S. Huang, X. R. Qi, D. H. Zhang and Y. S. Zhu, Phys. Rev. D **62**, 034003 (2000); R. L. Yang, R. G. Ping and H. Chen, Chin. Phys. Lett. **31**, 061301 (2014).
- [39] E. Richter-Was, Phys. Lett. B **303**, 163 (1993).
- [40] K. S. Cranmer, Comput. Phys. Commun. **136**, 198 (2001).
- [41] S. Eidelman and F. Jegerlehner, Z. Phys. C **67**, 585 (1995).
- [42] E. A. Kuraev and V. S. Fadin, Yad. Fiz. **41**, 733 (1985); [Sov. J. Nucl. Phys. **41**, 466 (1985)].
- [43] M. Ablikim *et al.* (BESIII Collaboration), Phys. Rev. D **83**, 112005 (2011).
- [44] M. Ablikim *et al.* (BESIII Collaboration), Phys. Rev. D **81**, 052005 (2010).
- [45] M. Ablikim *et al.* (BESIII Collaboration), Phys. Rev. D **87**, 052005 (2013).
- [46] C. F. Qiao, F. Yuan, and K. T. Chao, Phys. Rev. D **55**, 4001 (1997).
- [47] Qin-Rong Gong *et al.*, Eur. Phys. J. C **78**, 276 (2018).

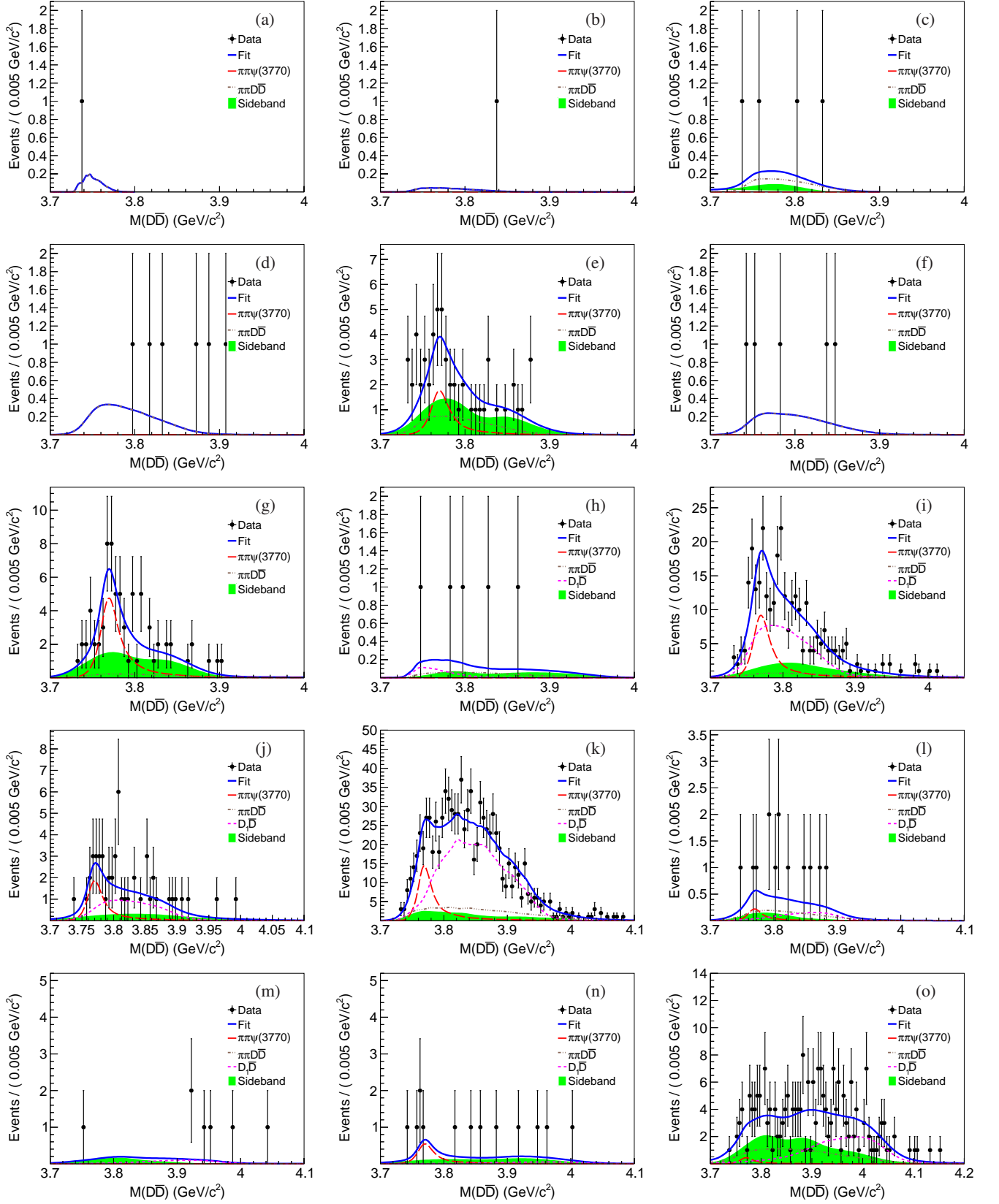
Appendix A: Fits to the $D\bar{D}$ invariant mass distributions

FIG. 8: Fit to the $D\bar{D}$ invariant mass distribution at $\sqrt{s} = 4.09$ (a), 4.19 (b), 4.21 (c), 4.22 (d), 4.23 (e), 4.245 (f), 4.26 (g), 4.31 (h), 4.36 (i), 4.39 (j), 4.42 (k), 4.47 (l), 4.53 (m), 4.575 (n) and 4.60 (o) GeV. The black dots with error bars are data and the blue solid lines are the fit results. The red long-dashed lines indicate the contribution of the $\psi(3770)$ and the pink dashed lines the contribution of the $D_1(2420)\bar{D}$ final state. The brown dotted-dashed lines show the $\pi^+\pi^-D\bar{D}$ background contributions and the green shaded histograms are the distributions from the sideband regions.

Appendix B: Fits to the $D\pi^+\pi^-$ invariant mass distributions

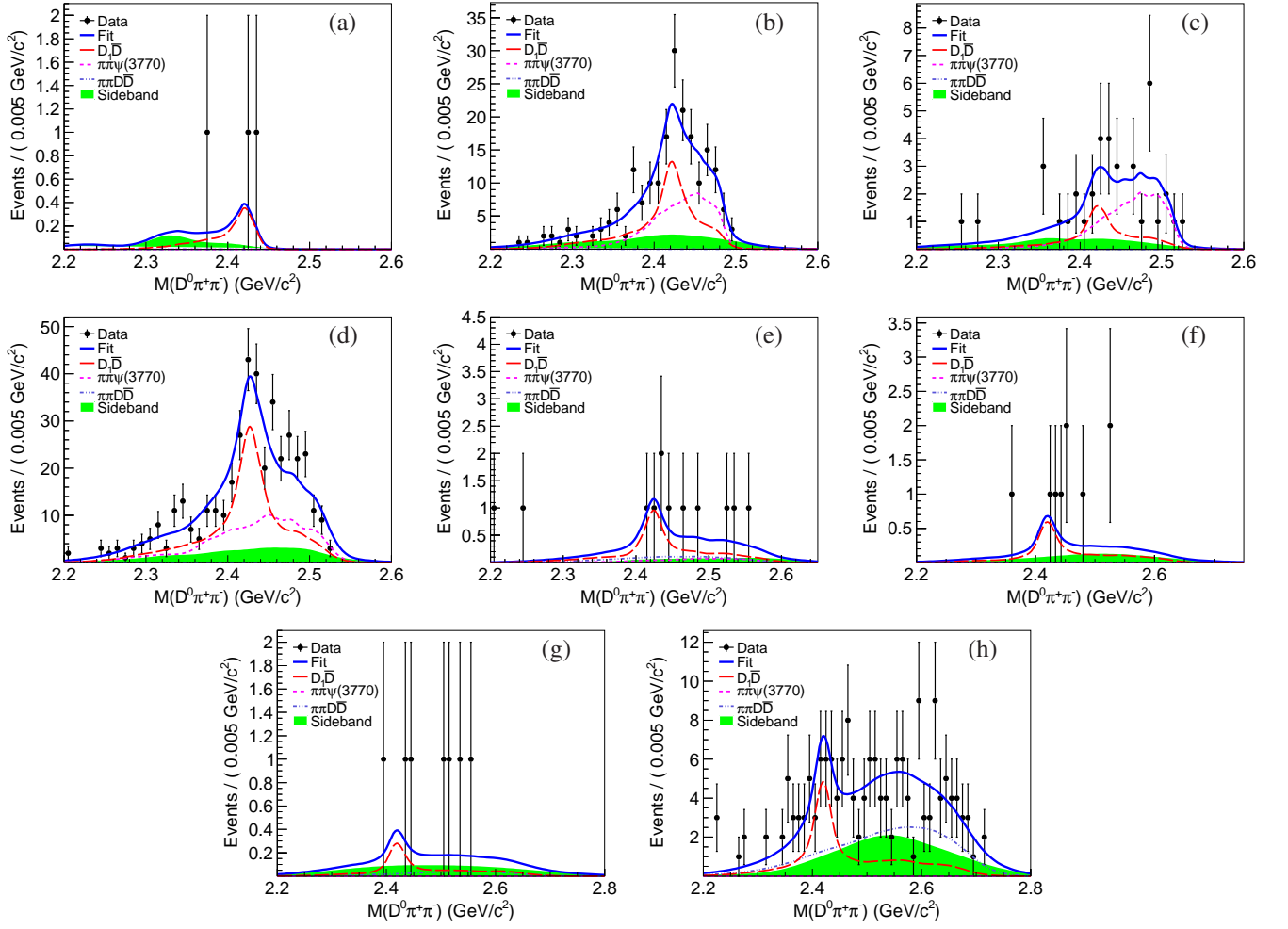


FIG. 9: Fit to the $D^0\pi^+\pi^-$ invariant mass distribution at $\sqrt{s} = 4.31$ (a), 4.36 (b), 4.39 (c), 4.42 (d), 4.47 (e), 4.53 (f), 4.575 (g) and 4.60 (h) GeV. The black dots with error bars are data, the blue solid curves the fits results, and the red long-dashed lines the $D_1(2420)$ signal contributions. The pink dashed lines are the contributions of the final state $\pi^+\pi^-\psi(3770)$ and the blue dot-dot-dashed lines these of the $\pi^+\pi^-D\bar{D}$ final state, while the green shaded histograms are the distributions from the sidebands regions.

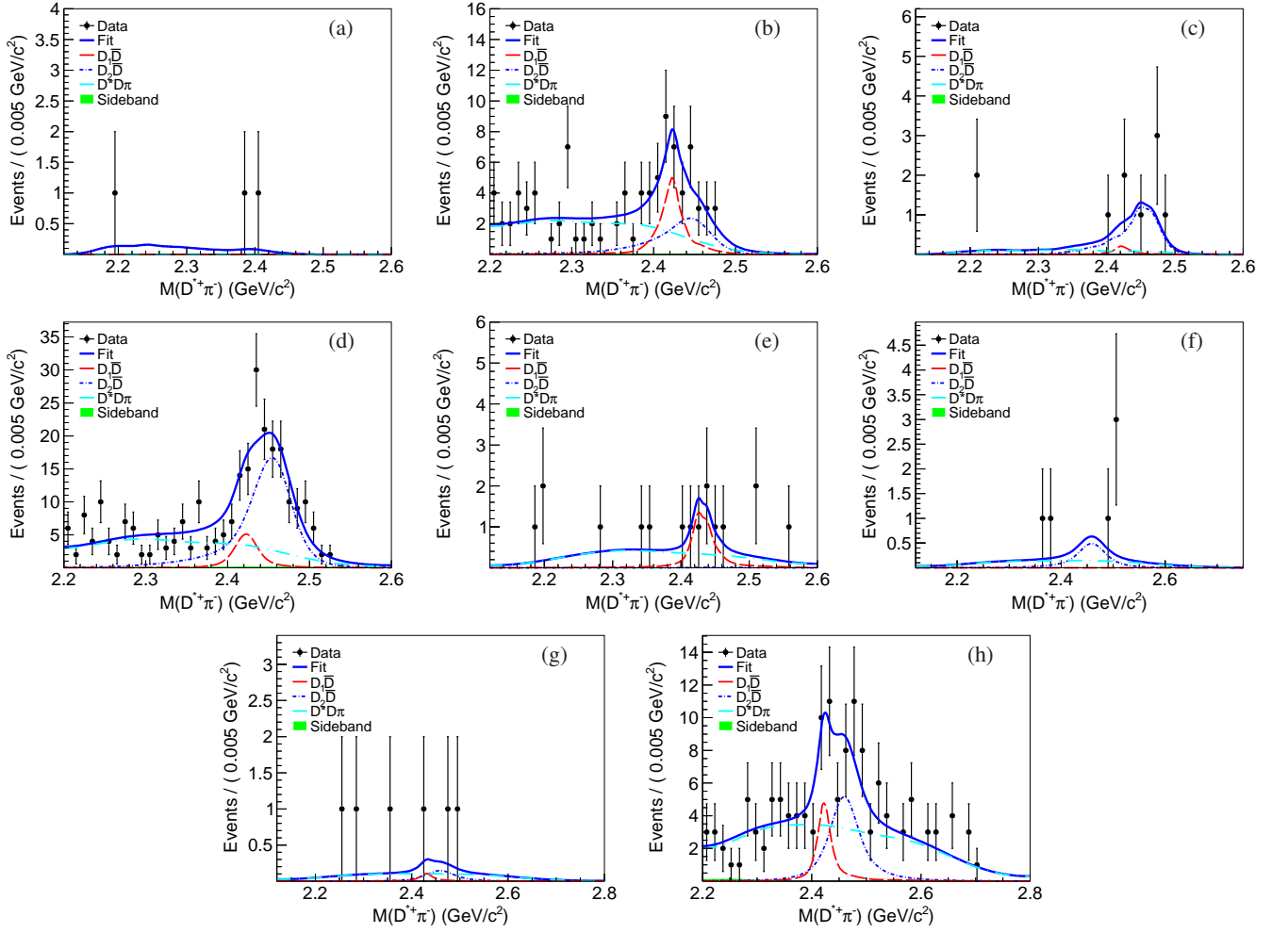


FIG. 10: Fit to the $D^{*+}\pi^-$ invariant mass distribution at $\sqrt{s} = 4.31$ (a), 4.36 (b), 4.39 (c), 4.42 (d), 4.47 (e), 4.53 (f), 4.575 (g) and 4.60 (h) GeV. The black dots with error bars are data, the blue solid curves the fit results, and the red long-dashed lines the $D_1(2420)$ signal contributions. The light blue dot-long-dashed lines are the $D^*\bar{D}\pi$ and the blue dot-dashed lines the $D_2^*(2460)^0\bar{D}\pi$ background contributions, while the green shaded histograms are the distributions from the sideband regions.

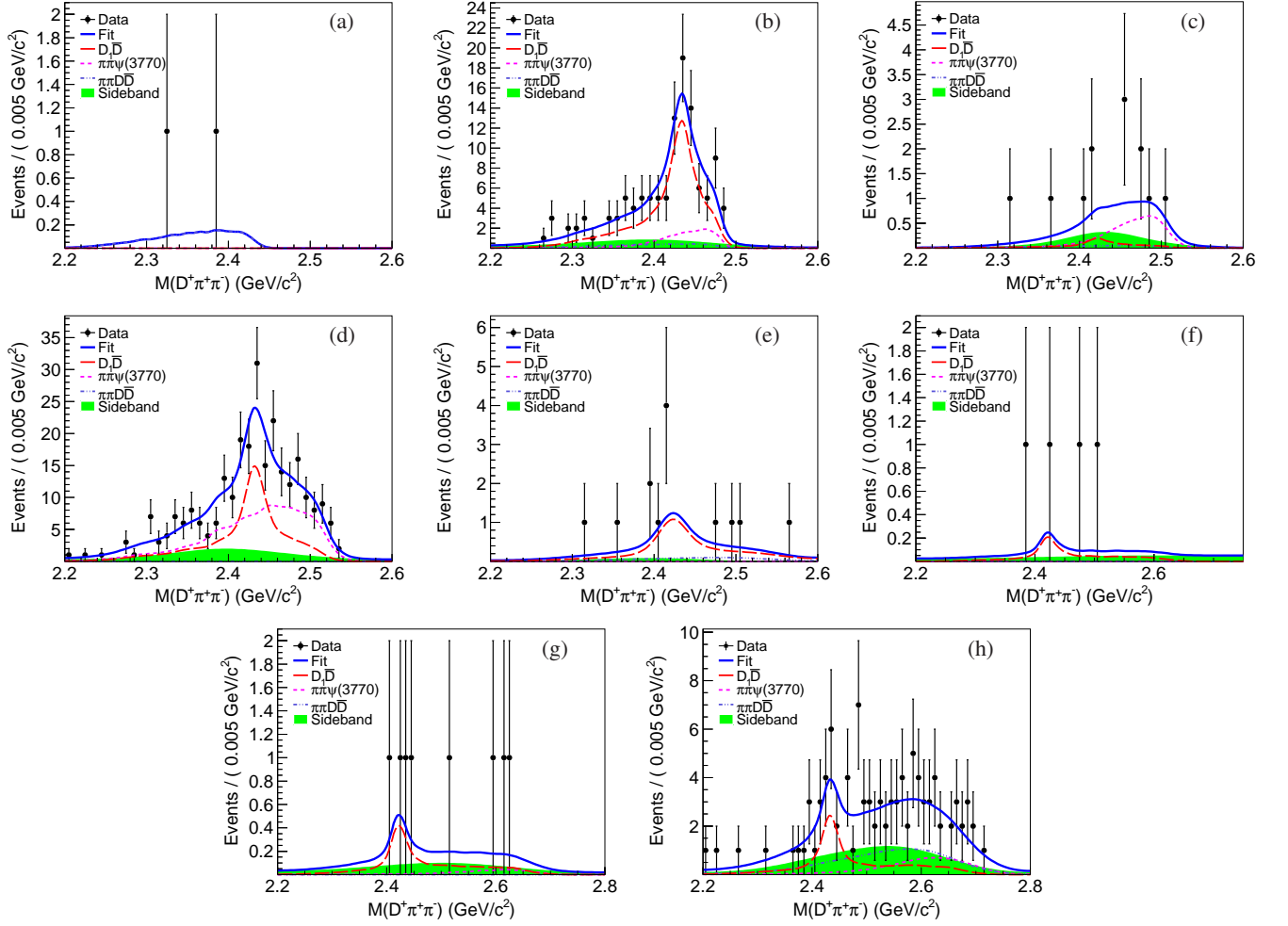


FIG. 11: Fit to the $D^+\pi^+\pi^-$ invariant mass distribution at $\sqrt{s} = 4.31$ (a), 4.36 (b), 4.39 (c), 4.42 (d), 4.47 (e), 4.53 (f), 4.575 (g) and 4.60 (h) GeV. The black dots with error bars are data, the blue solid curves the fit results, and the red long-dashed lines the $D_1(2420)$ signal contribution. The pink dashed lines are contributions of the final state $\pi^+\pi^-\psi(3770)$ and the blue dot-dot-dashed lines these of the $\pi^+\pi^-D\bar{D}$ final state, while the green shaded histograms are the distributions from the sideband regions.

Appendix C: Systematic uncertainties for the measurements of $\sigma(e^+e^- \rightarrow \pi^+\pi^-\psi(3770))$ and $\sigma(e^+e^- \rightarrow D_1(2420)^0\bar{D}^0)$

TABLE XI: Systematic uncertainties (in %) in $\sigma(e^+e^- \rightarrow \pi^+\pi^-\psi(3770))$ measurement.

Sources / \sqrt{s} (GeV)	4.0854	4.1886	4.2077	4.2171	4.2263	4.2417	4.2580	4.3079	4.3583	4.3874	4.4156	4.4671	4.5271	4.5745	4.5995
Integrated luminosity	1.0	1.0	1.0	1.0	1.0	1.0	1.0	1.0	1.0	1.0	1.0	1.0	1.0	1.0	1.0
Efficiency related	9.2	9.3	9.2	9.2	9.0	9.0	9.2	9.0	8.9	8.8	8.8	8.7	8.7	8.7	8.6
Radiative correction	1.3	1.5	2.1	1.5	0.6	4.4	1.1	6.3	0.6	1.8	2.1	1.8	0.7	2.5	0.2
Signal shape	3.4	3.4	3.4	3.4	3.4	3.4	3.4	3.4	3.4	3.4	3.8	3.8	3.8	3.8	3.8
Background shape	9.9	9.9	9.9	9.9	9.9	9.9	9.9	9.9	9.9	9.9	7.6	7.6	7.6	7.6	7.6
Fit range	2.0	2.0	2.0	2.0	2.0	2.0	2.0	2.0	2.0	2.0	2.4	2.4	2.4	2.4	2.4
Signal region of double tag	5.3	5.3	5.3	5.3	5.3	5.3	5.3	5.3	5.3	5.3	2.0	2.0	2.0	2.0	2.0
Total	14.3	15.2	15.2	15.1	15.0	15.6	15.1	16.2	14.9	15.0	12.8	12.7	12.6	12.8	12.5

TABLE XII: Relative systematic uncertainties (in %) in $\sigma(e^+e^- \rightarrow D_1(2420)^0 \bar{D}^0, D_1(2420)^0 \rightarrow D^0 \pi^+ \pi^- + c.c.)$ measurement.

Sources / \sqrt{s} (GeV)	4.3079	4.3583	4.3874	4.4156	4.4671	4.5271	4.5745	4.5995
Integrated luminosity	1.0	1.0	1.0	1.0	1.0	1.0	1.0	1.0
Efficiency related	12.4	12.4	12.3	12.2	12.1	12.1	12.1	12.0
Radiative correction	6.4	0.6	1.8	2.1	1.8	0.7	2.5	0.2
Signal shape	7.2	7.2	7.2	5.5	5.5	8.2	8.2	8.2
Background shape	3.2	3.2	3.2	1.2	1.2	7.4	7.4	7.4
Fit range	0.9	0.9	0.9	1.0	1.0	0.9	0.9	0.9
Signal region of double tag	2.6	2.6	2.6	4.2	4.2	4.8	4.8	4.8
$\sigma(\pi\pi\psi(3770))$	11.4	11.4	11.4	0.5	0.5	1.1	1.1	1.1
Total	19.9	18.8	18.8	14.3	14.2	17.1	17.3	17.0

TABLE XIII: Relative systematic uncertainties (in %) in $\sigma(e^+e^- \rightarrow D_1(2420)^0 \bar{D}^0, D_1(2420)^0 \rightarrow D^{*+} \pi^- + c.c.)$ measurement.

Sources / \sqrt{s} (GeV)	4.3079	4.3583	4.3874	4.4156	4.4671	4.5271	4.5745	4.5995
Integrated luminosity	1.0	1.0	1.0	1.0	1.0	1.0	1.0	1.0
Efficiency related	14.0	14.0	13.9	13.8	13.8	13.7	13.7	13.6
Radiative correction	6.3	0.6	1.8	2.1	1.8	0.7	2.5	0.2
Signal shape	5.3	5.3	5.3	2.8	2.8	4.9	4.9	4.9
Background shape	0.2	0.2	0.2	1.8	1.8	7.4	0.1	0.1
Fit range	2.7	2.7	2.7	3.9	3.9	0.8	0.8	0.8
Signal region of double tag	4.9	4.9	4.9	2.6	2.6	9.8	9.8	9.8
Total	17.2	16.0	16.1	15.1	15.1	19.1	17.7	17.5

TABLE XIV: Relative systematic uncertainties (in %) in $\sigma(e^+e^- \rightarrow D_1(2420)^+ D^-, D_1(2420)^+ \rightarrow D^+ \pi^+ \pi^- + c.c.)$ measurement.

Sources / \sqrt{s} (GeV)	4.3079	4.3583	4.3874	4.4156	4.4671	4.5271	4.5745	4.5995
Integrated luminosity	1.0	1.0	1.0	1.0	1.0	1.0	1.0	1.0
Efficiency related	13.5	13.4	13.3	13.2	13.1	13.1	13.1	13.0
Radiative correction	2.4	0.2	1.0	1.0	0.6	3.4	1.4	1.5
Signal shape	7.4	7.4	7.4	4.2	4.2	4.1	4.1	4.1
Background shape	1.6	1.6	1.6	0.8	0.8	3.8	3.8	3.8
Fit range	1.7	1.7	1.7	0.9	1.0	1.7	1.7	1.7
Signal region of double tag	1.1	1.1	1.1	1.3	1.3	5.2	5.2	5.2
$\sigma(\pi\pi\psi(3770))$	11.1	11.1	11.1	0.3	0.3	1.7	1.7	1.7
Total	19.3	19.1	19.1	14.0	13.9	15.8	15.5	15.4